Carbon 184 (2021) 923–940

Contents lists available at ScienceDirect

Carbon

journal homepage: www.elsevier.com/locate/carbon

Research Paper

Closed-form solutions for the piezoresistivity properties of short-fiber reinforced composites with percolation-type behavior

Federico C. Buroni [a, b, *], Enrique García-Macías [c]

[a] Escuela Técnica Superior de Ingeniería, Department of Mechanical Engineering and Manufacturing, Universidad de Sevilla, Camino de Los Descubrimientos S/n, 41092, Seville, Spain
[b] Escuela Politécnica Superior, Department of Mechanical Engineering and Manufacturing, Universidad de Sevilla, Calle Virgen de África 7, 41011, Seville, Spain
[c] Escuela Técnica Superior de Ingeniería de Caminos, Canales y Puertos, Universidad de Granada, Campus Universitario de Fuentenueva, Granada, 18071, Spain

ARTICLE INFO

Article history:
Received 5 July 2021
Received in revised form
26 August 2021
Accepted 30 August 2021
Available online 2 September 2021

Keywords:
Analytical effective properties
Carbon nanotube
Generalized spherical harmonics
Mean-field homogenization
Orientation distribution functions
Percolation

ABSTRACT

A new analytical formulation for the modeling of piezoresistive fiber-reinforced composites with percolation-type behavior is presented in this work. Firstly, we develop a closed-form solution of the electrical conductivity of oriented short-fiber reinforced composites by using generalized spherical harmonics series expansions of a Mori-Tanaka (MT) model. Piezoresistive effects are accounted for by means of three distinct mechanisms, namely filler reorientation, volume expansion, and breakage/formation of conductive paths. Then, this solution is used to derive simple analytical formulas to estimate the linear piezoresistivity coefficients. To illustrate the potentials of the proposed formulation, numerical results and discussion are presented on its application to the modeling of the piezoresistive composites doped with carbon nanotubes (CNTs). The presented formulation is also inlaid in a standard 3D finite element code to simulate the electromechanical response of full-scale CNT-based structural elements. The reported results demonstrate the capabilities of the proposed formulation to link the microstructural properties of short-fiber composites with the macroscopic response of structural systems with extraordinarily fast computation times and accuracy.

1. Introduction

Recent advances in the field of piezoresistive composites have opened vast new opportunities for the development of a number of innovative smart structures such as self-diagnostic structural systems [1], artificial skins in robotics [2], biomedical implants [3], soft electronics [4], and human motion detection [5], just to mention a few. In this context, carbon-based nanomaterials, including CNTs, graphene nanoplatelets (GNPs), carbon nanofibers (CNFs), carbon-black (CB), Graphene oxide (GO), and CNT bucky papers (CNT-BP), have attracted particular interest owing to their excellent electro-thermo-chemical properties [6]. When doped into an insulating or poorly conductive matrix material such as polymer or cement, the resulting composite becomes piezoresitive. The working principle of these composite materials lies in the formation of a network of electrically conductive fillers sensitive to the application of external mechanical strains. Hence, electrical resistivity measurements can be directly related to the underlying strain state of the material, being possible to manufacture mechanical load-bearing sensors. Given the far-reaching possibilities of these composites, there is an increasing need for accurate but computationally efficient and easily implementable constitutive models capable of investigating the macroscopic response of full-scale applications.

Large research efforts have been exerted to identify and characterize the electrical transport properties of these composites. In general, both theoretical and experimental evidences agree to attribute the electrical conductivity of carbon-based composites to three different contributions [6]: (*i*) the intrinsic conductivity of the constituent phases; (*ii*) the formation of electrically conductive paths between fibers; and (*iii*) tunneling/hopping of electrons among disconnected fibers. The relative contributions of conductive networking and electron hopping mechanisms are governed by a percolation-type behavior [7]. In this light, the overall electrical

* Corresponding author. Escuela Técnica Superior de Ingeniería, Department of Mechanical Engineering and Manufacturing, Universidad de Sevilla, Camino de los Descubrimientos s/n, 41092, Seville, Spain.
E-mail address: fburoni@us.es (F.C. Buroni).

https://doi.org/10.1016/j.carbon.2021.08.083

conductivity of these composites typically exhibits a sudden increase of several orders of magnitude when the filler loading reaches a critical concentration, named the percolation threshold. This critical concentration relates the onset of the conductive networking mechanism. Hence, the overall electrical conductivity below percolation is governed by the sole contribution of the electron hopping mechanism, while both conductive networking and electron hopping mechanisms contribute after percolation. A variety of modeling techniques to unveil the role of the microstructural properties of these composites in their overall electrical conductivity have been proposed in the literature. These include analytical percolation models [8,9], micromechanics approaches based upon the mean-field homogenization (MFH) theory [10–13], equivalent lumped-element circuit models [14–16], and numerical Monte Carlo simulation methods [17,18]. Then, the piezoresistive properties of these composites are ascribed to strain-induced alterations of these electrical transport mechanisms. Specifically, three distinct mechanisms are commonly highlighted in the literature [19–21]: (*i*) volume expansion, (*ii*) filler reorientation, and (*iii*) changes in the inter-particle properties. Among the research works coping with the simulation of such strain-induced effects, it is worth noting the pioneering works by Hu et al. [22] and Alamusi and Hu [23] who proposed a 3D resistor network model to estimate the piezoresistive properties of CNT/polymer composites. Following these contributions, most subsequent research works simulate the electrical contact resistance among CNTs following the generalized Simmon's formula [24]. Furthermore, many modeling approaches reported later include the fiber reorientation effects through different versions of the rigid-body reorientation model set out by Taya et al. [25]. A noteworthy contribution was made by Tallman and Wang [21] who proposed an analytical formulation based upon a simplified excluded volume approach for CNT-based composites under arbitrary dilations. Their results reproduced some of the experimental evidence on piezoresistive carbon-based composites. On one hand, the strain sensitivity of CNT-reinforced composites can be assimilated by a linear range followed by a non-linear one. On the other hand, those authors showed that both the strain sensitivity and the relevance of the non-linear effects increases as the CNT content approaches the percolation threshold. Another important contribution was due to Feng and Jiang [20,26] who proposed a mixed Mori-Tanaka MFH approach for the modeling of the uni-axial and bi-axial strain self-sensing properties of CNT/polymer composites. Later extended by García-Macías and co-authors [27] for arbitrary principal strains, this approach has proved proficient to include the main mechanisms leading the resistivity properties of CNT-based composites within an analytical and sound approach. Following these efforts, a considerable number of analytical [1,28,29,68] and numerical simulation techniques [30–32] for the modeling of the piezoresistivity properties of percolation-type composites have been recently proposed in the literature.

Amongst the previously mentioned modelling schemes, micromechanics approaches based upon the MFH theory offer an excellent trade off between accuracy and computational efficiency. The mean-field scheme solves the boundary value problem associated with the homogenization of composite materials in analytical terms. To do so, the micro-fields within each constituent (e.g. strain, stress, electric field or current density) are approximated by their volume averages [55]. Then, different assumptions upon the interaction between the micro-constituents give origin to different MFH techniques [66]. Specifically, the MT model has proved suitable for composite materials doped with moderate to low filler contents, finding a number of applications in the literature to elastic [69], electrically conductive [68], or piezoelectric composites [67], just to mention a few. The main advantage of MFH relies in the fact that estimates are formulated in analytic tensorial terms, allowing to establish functional relations between the micromechanical properties without involving computationally burdensome virtual testing of numerical representative volume elements (RVEs). In the realm of piezoresistive fiber-reinforced composites, these techniques have proved proficiency to reproduce the primary mechanisms governing the strain-sensing properties within a computationally inexpensive analytical framework and with minimal support from experimentation [20,27]. These include the consideration of volume expansion effects under the assumption of inextensible fillers, breakage/formation of conductive paths through variations of the percolation threshold, variation of the inter-particle properties, and filler-reorientation [10,13,25]. Feng and Jiang [20] extended the rigid-body reorientation theory by Taya et al. [25] and showed that filler reorientation effects can be simulated in mathematical terms by means of strain-dependent Orientation Distribution Functions (ODFs). Specifically, those authors presented closed-form expressions of the reorientation ODF for the case of laterally unconstrained axial stretching. Afterward, García-Macías and co-authors [27] proposed a generalization of these ODFs for the consideration of arbitrary principal strains. Interestingly, those authors also showed that these ODFs can be also used to estimate the effects of strain upon the percolation threshold through stochastic percolation models such as the one proposed by Komori and Makishima [33]. These probability density functions are used to weight the orientational averages involved in the MFH theory throughout the space of all filler orientations. Such orientational averages usually require the implementation of numerical integration techniques. These approximations introduce numerical integration errors and, more importantly, diminish the computational efficiency of the homogenization when applied to the analysis of macrostructural elements.

In view of the aforementioned limitations related to the MFH of piezoresistive fiber-reinforced composites, this work is aimed at developing a fully analytical approach based upon the closed-form integration of the kernels involved in the MT method through spherical harmonics expansions. According to the celebrated Peter-Weyl theorem [34], kernel functions belonging to the special orthogonal group can be expanded in generalized spherical harmonics series. Consequently, by exploiting the orthogonality properties of generalized spherical harmonics functions [35], integral averaging can be conducted in a direct way by the harmonic series expansion method [36,37]. This powerful technique has been successfully applied in several works to estimate the effective properties of composite materials, mainly for textured polycrystals [38–42] and short-fiber composites [43–45], as well as some recent applications to composites with piezoelectric polycrystalline inclusions [46–51]. In this light, the harmonic series expansion method is used in this work to derive a closed-form formulation of the electrical conductivity and piezoresistivity of random fiber/matrix composites. The proposed approach incorporates the major microstructural properties of piezoresistive composites with percolation-type behavior, including the geometrical and physical properties of the constituents, percolative and non-percolative phases, as well as strain sensitivity through three distinct mechanisms, namely filler reorientation, volume expansion, and breakage/formation of conductive paths. Thanks to its closed-form definition and for the first time in the literature, simple explicit formulas of the piezoresistivity coefficients of percolative and non-percolative composites with arbitrarily shaped inclusions are derived by direct linearization of the proposed formulation. To illustrate the potentials of the present formulation, numerical results and discussion are presented on its application to the modeling of CNT-based composites. Finally, the proposed approach is also implemented in a standard 3D finite element code to

simulate the electromechanical response of a full-scale CNT-based structural element, reporting extraordinarily fast computation times and accuracy. Computer codes in MATLAB and Python languages with the implementation of the developed formulation are provided in Supplementary Material 2 as an open-source tool for the scientific community.

The work is organized as follows. Section 2 introduces a micromechanical model for electrical conductivity of random fiber composites accounting for the percolation phenomenon. In Section 3 we develop an analytical solution for the composite conductivity by using generalized spherical harmonics series expansions. In this light, we provide all the components for the effective conductivity tensor in terms of the strain state and the volume fraction, micro-conductivities and aspect ratio of the filler. Section 4 presents simple algebraic expressions for the linear piezoresistive constants, including the possibility that fibers form percolating networks. In Section 5, the derived formulation is illustrated in detail with its application to the modeling of CNT-based composites, and Section 6 summarizes the key findings and conclusions of this work. Additional contributions are presented in the supplementary materials.

2. Micromechanical model for conductivities

Let us consider a RVE as sketched in Fig. 1 (a) consisting of a matrix phase and a statistically representative population of randomly oriented cylindrical inclusions. In general, the orientation of each inclusion with respect to a fixed reference x_i ($i = 1, 2, 3$) can be described with three Euler angles ψ, θ, and φ following the convention used by Roe [52]. According to the percolation theory, the electrical conductivity of the composite experiences an expeditious increase when the filler content reaches a critical concentration, the so-termed percolation threshold f_c. Below percolation, fillers are distant and electrons can only be transferred by quantum tunneling effects or through the matrix phase (in general, considerably less conductive than the fillers). Above the percolation threshold, fillers can touch each other forming micro-scale electrically conductive paths. The use of MFH, while based upon some simplifying assumptions, allows to estimate the effective properties of these composites with reasonable computational costs. In particular, the MT method [53] has been shown accurate to estimate the effective properties of composites doped with a wide variety of inclusions at low to moderate filler concentrations. In this light, a multi-inclusion non-linear extension of the MT method has been previously proposed in the literature to accommodate the contribution of both percolated and non-percolated inclusions as [13,19]:

$$\boldsymbol{\sigma}(\boldsymbol{\varepsilon}) = \boldsymbol{\sigma}_m + \underbrace{(1-\xi(\boldsymbol{\varepsilon}))\langle f(\boldsymbol{\varepsilon})(\boldsymbol{\sigma}_{NP}(\boldsymbol{\varepsilon}) - \boldsymbol{\sigma}_m)\boldsymbol{A}_{NP}(\boldsymbol{\varepsilon})\rangle}_{\text{Non-percolating}} + \underbrace{\xi(\boldsymbol{\varepsilon})\langle f(\boldsymbol{\varepsilon})(\boldsymbol{\sigma}_P(\boldsymbol{\varepsilon}) - \boldsymbol{\sigma}_m)\boldsymbol{A}_P(\boldsymbol{\varepsilon})\rangle}_{\text{Percolating}}, \tag{1}$$

where the first term, $\boldsymbol{\sigma}_m$, is the conductivity tensor of the matrix, which is represented —assuming isotropic behavior— by a diagonal matrix $\sigma_m\delta_{ij}$ ($i, j = 1\ldots3$), with δ_{ij} denoting the Kronecker delta. Second and third terms account for the non-percolating and the percolating mechanisms, respectively. Thus, $\boldsymbol{\sigma}_{NP}$ and $\boldsymbol{\sigma}_P$ are the conductivity tensors of the fibres which, in this work, are considered as transversely isotropic. Operator $\langle\bullet\rangle$ is the orientation average of the fibres weighted by an orientation probability density function, which is rigorously defined below. Term $\xi(\boldsymbol{\varepsilon})$ denotes the fraction of percolated fillers, that is to say, the fraction of fillers touching each other forming conductive microscopic paths. As previously indicated, the overall conductivity of composites loaded with fibre volume fractions below the percolation threshold, $f(\boldsymbol{\varepsilon}) < f_c(\boldsymbol{\varepsilon})$, the non-percolating mechanism governs the overall conductivity of the composite and, therefore, the fraction of percolated fibres, $\xi(\boldsymbol{\varepsilon})$, is null. Conversely, once percolation starts, $f(\boldsymbol{\varepsilon}) \geq f_c(\boldsymbol{\varepsilon})$, a rising number of fibres starts forming conductive networks and both the percolating and the non-percolating mechanisms act simultaneously. Provided a model for $f_c(\boldsymbol{\varepsilon})$ (see Section 4.2), parameter $\xi(\boldsymbol{\varepsilon})$ can be approximately estimated as [54]:

$$\xi(\boldsymbol{\varepsilon}) = \begin{cases} 0, & 0 \leq f(\boldsymbol{\varepsilon}) < f_c(\boldsymbol{\varepsilon}) \\ \dfrac{f(\boldsymbol{\varepsilon})^{1/3} - f_c^{1/3}(\boldsymbol{\varepsilon})}{1 - f_c^{1/3}(\boldsymbol{\varepsilon})}, & f_c(\boldsymbol{\varepsilon}) \leq f(\boldsymbol{\varepsilon}) \leq 1. \end{cases} \tag{2}$$

Tensors $\boldsymbol{A}_{NP}$ and $\boldsymbol{A}_P$ in Eq. (1) denote the concentration tensors. When conductive networks mechanism starts, several fibres are electrically connected in a continuous conductive path as sketched in Fig. 1 (a). This effect can be modeled by considering fillers with

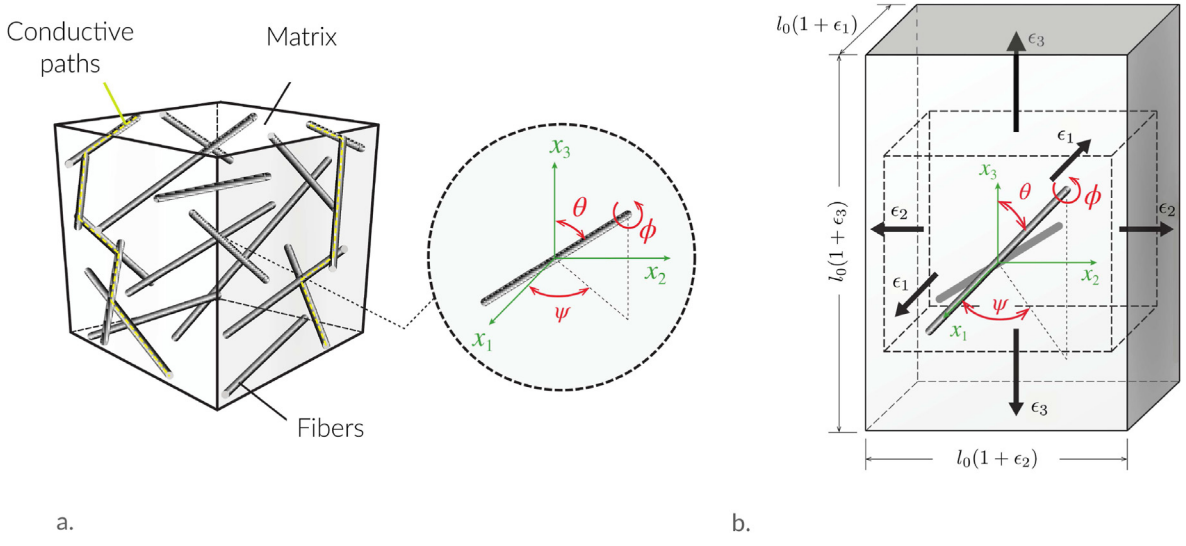

a. b.

Fig. 1. (a) Schematic of the conductive mechanisms governing the electrical conductivity of fiber-reinforced composite. (b) Deformable cubic cell of size $l_0 \times l_0 \times l_0$ containing an embedded filler under a tri-axial strain state (ε_1, ε_2, ε_3). (A colour version of this figure can be viewed online.)

infinite aspect ratio s (length-to-diameter) [13]. Therefore, $\boldsymbol{A}_{NP}$ is computed considering the actual filler's aspect ratio, while $\boldsymbol{A}_P$ tensor corresponding to conductive networks are defined with $s \to \infty$ as detailed before. The concentration tensor $\boldsymbol{A}$ is computed by Ref. [45].

$$\boldsymbol{A} = \boldsymbol{A}^{\text{dil}}\Big((1-f)\mathbf{I} + f\boldsymbol{A}^{\text{dil}}\Big)^{-1}, \tag{3}$$

with

$$\boldsymbol{A}^{\text{dil}} = \Big(\boldsymbol{I} + \boldsymbol{S}\boldsymbol{\sigma}_m^{-1}\Big(\boldsymbol{\sigma}_f - \boldsymbol{\sigma}_m\Big)\Big)^{-1}, \tag{4}$$

where $\boldsymbol{I}$ is the 3×3 identity matrix and $\boldsymbol{S}$ is the shape-dependent Eshelby's tensor. For transversely isotropic fibers aligned with local x_3'-axis, conductivity is $\boldsymbol{\sigma}_f = \text{diag}(\sigma^T, \sigma^T, \sigma^L)$ and $\boldsymbol{S} = \text{diag}(S_{11}, S_{11}, S_{33})$ with components [55].

$$S_{11} = \frac{s}{2(s^2-1)^{\frac{3}{2}}}\left[s\Big(s^2-1\Big)^{\frac{1}{2}} - \cosh^{-1}(s)\right], \tag{5}$$

and

$$S_{33} = 1 - 2S_{11}, \tag{6}$$

being s ($s > 1$) the aspect ratio length-to-diameter of the fiber.

Note that the dependency on the small strain tensor, $\boldsymbol{\varepsilon}$, in the MT's model in Eq. (2) results in non-linearities in the strain-induced variations of the effective electrical conductivity. Thus, a key point to achieve accurate estimates of the piezoresistivity properties is to establish the influence of external strains upon three different aspects: (*i*) mechanical strains alter the volume of the composite which modifies the volume fraction of the fillers f and, as a result, the fraction of percolated fibers ξ from Eq. (2); (*ii*) fillers experience reorientation, which modifies the spatial distribution of the fibers and, in consequence, introduces anisotropy in the conductivity; and (*iii*) as a result of the latter mechanism, external strains also modify the percolation threshold. Note that the reorientation of the fillers decreases the randomness of the filler distribution which, as discussed in further details hereafter, can be formally described by an Orientation Distribution Function (ODF). An ODF is a probability density function (PDF) describing the orientation of the fillers in the composite in probabilistic terms. In this light, the work by Kumar and Rawal [59] demonstrated that minimum percolation thresholds are attained for randomly oriented fillers (uniform ODF), while the percolation threshold increases as the fillers tend to align in a certain preferred orientation. Therefore, it can be concluded that the reorientation of the fillers reduces the likelihood of forming conductive paths or, alternatively, it leads to increments in the percolation threshold f_c.

It is assumed that the filler remains inextensible since it is often considerably stiffer than that host matrix. In this way, the deformation of the composite is mainly sustained by the matrix and, therefore, the strain-induced volume expansion alters the unstrained fibre volume fraction f_0 as follows [10]:

$$f(\boldsymbol{\varepsilon}) = \frac{f_0}{\bar{\varepsilon}_1\bar{\varepsilon}_2\bar{\varepsilon}_3} = \frac{f_0}{\text{tr}(\boldsymbol{\varepsilon}) + \det(\boldsymbol{\varepsilon})\text{tr}(\boldsymbol{\varepsilon}^{-1}) + \det(\boldsymbol{\varepsilon}) + 1}, \tag{7}$$

with $\bar{\varepsilon}_1 = \varepsilon_1 + 1$, $\bar{\varepsilon}_2 = \varepsilon_2 + 1$ and $\bar{\varepsilon}_3 = \varepsilon_3 + 1$ being ε_1, ε_2 and ε_3 the three principal strains; $\det(\bullet)$ and $\text{tr}(\bullet)$ denote the determinant and trace operators, respectively. Note that $f(\boldsymbol{\varepsilon})$ is a function invariant under orthogonal transformations and it accounts for second-order volume changes.

The fiber reorientation is also modeled under the assumption that the filler is considerably stiffer than the matrix, so it remains inextensible [10]. Such an assumption allows to simulate the strain-induced reorientation of the fillers in the RVE following the deformable cubic cell model proposed by Taya et al. [25] and Feng and Jiang [20] for uni-axial strain states and later extended for three-dimensional (3D) strain states by García-Macías et al. [10]. According to this model, let us consider a deformable cubic cell of side l_0 loaded with an embedded fiber before and after the application of a 3D principal strain state (ε_1, ε_2, ε_3) as shown in Fig. 1 (b). The orientation of the fiber $\mathcal{D}_\alpha$ after the application of the mechanical strain is defined by a rotation $\mathbf{R}_\alpha$ from its initial orientation with respect to the fixed reference x_i (i = 1, 2, 3). In this light, the distribution of filler orientations after the application of a mechanical strain can be mathematically described by an ODF. This function is defined such as $w : SO(3) \to \mathbb{R}_{\geq 0}$, $\mathbf{R} \mapsto w(\mathbf{R})$ describes the probability density of finding $\mathbf{R}$ to be the fiber orientation after the application of the macroscopic deformation. The term $\mathbb{R}_{\geq 0}$ denotes the set of positive real numbers including zero and $SO(3)$ is the special orthogonal group. In this work, $SO(3)$ is parametrized with the three Euler angles $g = (\psi, \theta, \varphi)$. Following García-Macías et al. [10] the ODF after the application of deformations characterized by the principal strains is given in term of Euler's angles by:

$$w(\bar{\varepsilon}_1, \bar{\varepsilon}_2, \bar{\varepsilon}_3|\psi, \theta) = \frac{\bar{\varepsilon}_1^2\bar{\varepsilon}_2^2\bar{\varepsilon}_3^2}{\left[\bar{\varepsilon}_1^2\bar{\varepsilon}_2^2\cos^2\theta + \bar{\varepsilon}_3^2\Big(\bar{\varepsilon}_1^2\sin^2\psi + \bar{\varepsilon}_2^2\cos^2\psi\Big)\sin^2\theta\right]^{3/2}}. \tag{8}$$

Note that the geometrical revolution symmetry of fiber implies that w is independent of the third Euler's angle φ. In addition, the ODF in Eq. (8) takes the value 1 in the absence of strains ($\varepsilon_1 = \varepsilon_2 = \varepsilon_3 = 0$), which —after appropriate normalization— corresponds to the initial assumption of randomly dispersed fillers in the RVE.

3. Analytical solution for conductivities

While the previous formulation is presented in analytical terms, the orientational averages in Eq. (1) require the implementation of numerical integration techniques given the dependency upon the Euler angles provided by the ODF in Eq. (8). This numerical integration slows down the estimation of the effective electrical properties of the composite, and suffers from numerical integration errors. In order to tackle these limitations, this section presents an analytical solution of Eq. (1) by means of a generalized spherical harmonics series expansion of the previously introduced MT model. To this aim, let us recast the orientational averages of the tensors in Eq. (1) as follows:

$$\langle f\Big(\boldsymbol{\sigma}_f - \boldsymbol{\sigma}_m\Big)\boldsymbol{A}\rangle = \langle\boldsymbol{\Sigma}\rangle. \tag{9}$$

The orientational average in equation (9) is defined by the integration over the rotation group as

$$\langle\boldsymbol{\Sigma}\rangle := 8\pi^2 \int_{SO(3)} \boldsymbol{\Sigma}(g)w(g)\text{d}g, \tag{10}$$

where the ODF w is normalized such as

$$8\pi^2 \int_{SO(3)} w(g)\text{d}g = 1. \tag{11}$$

According to the transformation law for second-order tensors, $\boldsymbol{\Sigma}$

in the global coordinate system x_i ($i = 1\ldots3$) can be expressed in terms of the components of $\boldsymbol{\Sigma}$ for a fiber fixed to the x'_3-axis of the local coordinate system x'_i ($i = 1\ldots3$) as

$$\Sigma_{ij}(g) = \Omega_{im}(g)\Omega_{jn}(g)\Sigma'_{mn}, \tag{12}$$

where the components of $\boldsymbol{\Omega}$ in terms of the Euler angles is

$$\boldsymbol{\Omega}(\psi,\theta) = \begin{pmatrix} \cos\theta\cos\psi & -\sin\psi & cos\psi\, sin\theta \\ \cos\theta\sin\psi & \cos\psi & \sin\theta\sin\psi \\ -\sin\theta & 0 & \cos\theta \end{pmatrix}, \tag{13}$$

with $0 \le \psi < 2\pi$ and $0 \le \theta \le \pi$. By substituting Eq. (12) into (10), and with variable change, $\zeta := \cos\theta$, the components of the average in terms of (ψ, ζ, φ) are

$$\langle \Sigma_{ij} \rangle = \int_0^{2\pi}\int_0^{2\pi}\int_{-1}^{+1} w(\zeta,\psi)\Omega^{\otimes 2}_{imjn}(\zeta,\psi)\mathrm{d}\zeta\mathrm{d}\psi\mathrm{d}\varphi\, \Sigma'_{mn} = \left\langle \Omega^{\otimes 2}_{imjn} \right\rangle \Sigma'_{mn}, \tag{14}$$

where we have applied the normalized Haar measure dg in the Euler's space given by

$$\mathrm{d}g = \frac{1}{8\pi^2}\sin\theta\ \mathrm{d}\theta\mathrm{d}\psi\mathrm{d}\varphi, \tag{15}$$

which ensures invariant integration over the rotation group. The fourth-order matrix $\boldsymbol{\Omega}^{\otimes 2}$ condenses the dyadic product of $\boldsymbol{\Omega}$ in (12), and it possesses major symmetries only (minor symmetries are not present because $\boldsymbol{\Omega}$ is non-symmetric). Thus, the average $\langle \boldsymbol{\Sigma} \rangle$ can be computed once the average of each of the components $\langle \Omega^{\otimes 2}_{imjn} \rangle$ is obtained.

It is well-known [35] that generalized spherical harmonics

$$T_l^{mn}(\psi,\theta,\varphi) := e^{-\mathrm{i}m\psi} P_l^{mn}(\cos\theta) e^{-\mathrm{i}n\varphi}, \tag{16}$$

form a complete orthogonal basis for the Hilbert space $L^2(SO(3))$, which is the set of all square integrable complex-valued functions on the rotation group with inner product defined by

$$(F_1, F_2) = \int_{SO(3)} F_1(g)F_2^*(g)\mathrm{d}g,\ F_1, F_2 \in L^2(SO(3)), \tag{17}$$

where * denotes the complex conjugate. In definition (16), $\mathrm{i} = \sqrt{-1}$ and

$$P_l^{mn}(\zeta) = \frac{(-1)^{l-m}\mathrm{i}^{n-m}}{2^l(l-m)!}\left[\frac{(l-m)!(l+n)!}{(l+m)!(l-n)!}\right]^{\frac{1}{2}} \times \frac{(1-\zeta)^{\frac{-(n-m)}{2}}}{(1+\zeta)^{\frac{(n+m)}{2}}}\frac{d^{l-n}}{d\zeta^{l-n}}\left[(1-\zeta)^{l-m}(1+\zeta)^{l+m}\right], \tag{18}$$

is the associated Legendre function which can be either real or purely imaginary, according to whether $m + n$ is even or odd, respectively. Then, a generalization of the function P_l^{mn} can be expressed as [52].

$$Z_{lmn}(\zeta) := \mathrm{i}^{n-m}\sqrt{\frac{2l+1}{2}}P_l^{mn}(\zeta), \tag{19}$$

which is always real-valued. Hence, it is simple to show that $e^{-\mathrm{i}m\psi}Z_{lmn}(\zeta)e^{-\mathrm{i}n\varphi}$ form a complete orthogonal basis for the subspace of square integrable real-valued functions of $SO(3)$. Thus, according to the Peter-Weyl theorem [34], both a general ODF $w(\zeta, \psi, \varphi)$ and a general real function $F(\zeta, \psi, \varphi)$ can be expanded in series of generalized spherical harmonics as follows [52]:

$$w(\zeta,\psi,\varphi) = \sum_{l=0}^{\infty}\sum_{m=-l}^{l}\sum_{n=-l}^{l} W_{lmn}Z_{lmn}(\zeta)e^{-\mathrm{i}m\psi}e^{-\mathrm{i}n\varphi}, \tag{20}$$

and

$$F(\zeta,\psi,\varphi) = \sum_{l=0}^{\infty}\sum_{m=-l}^{l}\sum_{n=-l}^{l} F_{lmn}Z_{lmn}(\zeta)e^{-\mathrm{i}m\psi}e^{-\mathrm{i}n\varphi}. \tag{21}$$

Applying inner product (17), the coefficients of the expansions in Eqs. (20) and (21) are [37,52].

$$W_{lmn} = \frac{1}{4\pi^2}\int_0^{2\pi}\int_0^{2\pi}\int_{-1}^{+1} w(\zeta,\psi,\varphi)Z_{lmn}(\zeta)e^{\mathrm{i}m\psi}e^{\mathrm{i}n\varphi}\mathrm{d}\zeta\mathrm{d}\psi\mathrm{d}\varphi, \tag{22}$$

the so-called *texture coefficients*, and

$$F_{lmn} = \frac{1}{4\pi^2}\int_0^{2\pi}\int_0^{2\pi}\int_{-1}^{+1} F(\zeta,\psi,\varphi)Z_{lmn}(\zeta)e^{\mathrm{i}m\psi}e^{\mathrm{i}n\varphi}\mathrm{d}\zeta\mathrm{d}\psi\mathrm{d}\varphi. \tag{23}$$

All the information about the ODF is contained in the texture coefficients, which are complex quantities satisfying

$$W_{lmn} = (-1)^{m+n}W^*_{l\overline{m}n}, \tag{24}$$

due to the symmetry properties of $Z_{lmn}(\zeta)$ [52]. In Eq. (24), notation $\overline{m} = -m$ is adopted.

From the normalization condition (11), the first (untexture) coefficient become

$$W_{000} = \frac{1}{4\sqrt{2}\pi^2}. \tag{25}$$

Expansion coefficients F_{lmn} are complex and typically involve integration of simple trigonometric functions and the generalized spherical harmonics.

The most remarkable aspect of this theory is that the average of a general real function $\langle F \rangle$ can simply be computed by the expansion [36,37].

$$\langle F \rangle = 4\pi^2\sum_{l=0}^{R}\sum_{m=-l}^{l}\sum_{n=-l}^{l} F_{lmn}W_{lmn}, \tag{26}$$

where —from the truncation theorem by Ferrari and Johnson [42]— $R = 2$, i.e. the rank of $\boldsymbol{\Sigma}$. Then, for each of the real functions that are components of $\boldsymbol{\Omega}^{\otimes 2}$, their average can be computed by expansions similar to the one in Eq. (26). Therefore, we compute the corresponding coefficients F_{lmn} for each of the $\boldsymbol{\Omega}^{\otimes 2}_{imjn}$ in Eq. (14) through Eq. (23); and the texture coefficients W_{lmn} for the ODF given by Eq. (8) through Eq. (22). The property (24) has been used to simplify the expressions to their real form. Finally, we obtain that the non-zero components of the effective conductivity obtained from an homogenization method with structure like $\boldsymbol{\sigma} = \boldsymbol{\sigma}_m + \langle \boldsymbol{\Sigma} \rangle$, are given by

$$\sigma_{11} = \sigma_m + \frac{1}{15}\Big(4\sqrt{5}\,\pi^2(\Sigma_{11}-\Sigma_{33})\Big(\sqrt{2}\,W_{200} - 2\sqrt{3}\,W_{220}\Big) + 5(2\Sigma_{11}+\Sigma_{33})\Big), \tag{27}$$

$$\sigma_{22} = \sigma_m + \frac{1}{15}\Big(4\sqrt{5}\,\pi^2(\Sigma_{11}-\Sigma_{33})\Big(\sqrt{2}\,W_{200} + 2\sqrt{3}\,W_{220}\Big) + 5(2\Sigma_{11}+\Sigma_{33})\Big), \tag{28}$$

and

$$\sigma_{33} = \sigma_m + \frac{1}{15}\Big(8\sqrt{10}\,\pi^2 W_{200}(\Sigma_{33}-\Sigma_{11}) + 5(2\Sigma_{11}+\Sigma_{33})\Big) \tag{29}$$

It can be shown that W_{200} and W_{220} are real functions and, furthermore, they are the only two non-zero texture coefficients for the ODF in Eq. (8), whose explicit expressions are presented in the next subsection. Indeed, $\langle\boldsymbol{\Sigma}\rangle$ tensor is a diagonal matrix since $W_{210} = 0$, so no cross conductivity can be induced by the principal strains.

Note that effective conductivities have, in general, orthotropic symmetry according to the three modes of principal deformation. In case that the deformation is such that texture coefficient W_{220} vanishes, symmetry reduces to transversely isotropic with the axis of isotropy corresponding to the principal strain $\bar{\varepsilon}_3$. This is the case for deformations such as $\bar{\varepsilon}_1 = \bar{\varepsilon}_2$. (Note that this is not the only case. There are very particular combinations of deformations that also produce $W_{220} = 0$, however they are not of particular interest in this work). Alternatively, if $\bar{\varepsilon}_2 = \bar{\varepsilon}_3$, then $W_{220} = \sqrt{3/2}W_{200}$ and the isotropy axis is given by $\bar{\varepsilon}_1$; and if $\bar{\varepsilon}_1 = \bar{\varepsilon}_3$, then $W_{220} = -\sqrt{3/2}W_{200}$ and the isotropy axis is given by $\bar{\varepsilon}_2$. When no deformation takes place, that is, $\bar{\varepsilon}_1 = \bar{\varepsilon}_2 = \bar{\varepsilon}_3 = 1$, texture coefficients become null, $W_{200} = W_{220} = 0$, and hence the behavior is isotropic as expected, and the effective conductivity is given by the product of the identity matrix by the scalar

$$\sigma_0 = \sigma_m + \frac{1}{3}(2\Sigma_{11}+\Sigma_{33}). \tag{30}$$

It is worth noting that Dunn and Ledbetter [45] solved this problem for textured short-fiber composites in the context of thermal conductivity using the same mathematical technique proposed herein. Nevertheless, those authors presented no final expression.

Expressions (27)–(30) are the building blocks for the construction of analytical solutions for more complex MT's models like the one previously introduced in Eq. (1).

3.1. Determination of W_{200} and W_{220}

In order to have a fully analytical solution for the conductivities, it is necessary to determine an analytical solution for the texture coefficients. As previously mentioned, the only two non-zero texture coefficients for the ODF in Eq. (8) are W_{200} and W_{220}, which can be computed by integration of the function $w(\bar{\varepsilon}_1,\bar{\varepsilon}_2,\bar{\varepsilon}_3|\psi,\theta)$ — equation (8) after normalization (11)— in equation (22). Since we are interested in small strains, the strategy to compute this integrals is to expand the kernels in Taylor's series around $\bar{\varepsilon}_1 = \bar{\varepsilon}_2 = \bar{\varepsilon}_3 = 1$. This allows us to find closed-form expressions for the texture coefficients, $W_{200}^{(n)}$ and $W_{220}^{(n)}$, with various orders of approximation by retaining the desired n-th order terms, $(\bar{\varepsilon}_1-1)^n$, $(\bar{\varepsilon}_2-1)^n$ and $(\bar{\varepsilon}_3-1)^n$, in the Taylor's expansions. First-order approximation for texture coefficients results in

and

$$W_{200}^{(1)} = -\frac{\mathrm{i}\bar{\varepsilon}_1\bar{\varepsilon}_2\bar{\varepsilon}_3^2\sqrt{\bar{\varepsilon}_1^2\bar{\varepsilon}_2^2}(-16\bar{\varepsilon}_3(\bar{\varepsilon}_1+\bar{\varepsilon}_2)+\bar{\varepsilon}_1(32\bar{\varepsilon}_2-23)-23(\bar{\varepsilon}_2-2\bar{\varepsilon}_3))}{28\sqrt{10}\pi\left(\log\left(-\frac{\mathrm{i}\bar{\varepsilon}_1}{\bar{\varepsilon}_2}\right)-\log\left(\frac{\mathrm{i}\bar{\varepsilon}_1}{\bar{\varepsilon}_2}\right)\right)}, \tag{31}$$

$$W_{220}^{(1)} = \frac{\mathrm{i}\sqrt{\frac{3}{5}}\bar{\varepsilon}_1\bar{\varepsilon}_2\bar{\varepsilon}_3^2(16\bar{\varepsilon}_3-23)(\bar{\varepsilon}_1-\bar{\varepsilon}_2)\sqrt{\bar{\varepsilon}_1^2\bar{\varepsilon}_2^2}}{56\pi\left(\log\left(-\frac{\mathrm{i}\bar{\varepsilon}_1}{\bar{\varepsilon}_2}\right)-\log\left(\frac{\mathrm{i}\bar{\varepsilon}_1}{\bar{\varepsilon}_2}\right)\right)}. \tag{32}$$

The second-order approximation, instead, results in

and

All the integrals have been done using Mathematica software [56].

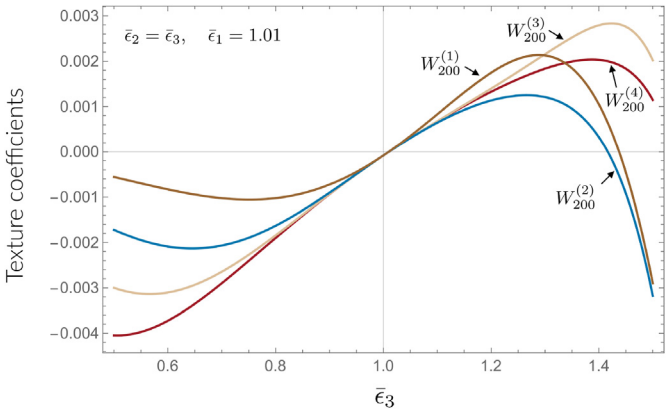

Fig. 2. Texture coefficient, $W_{200}^{(n)}$, of n-th order for the strain state $\bar{\varepsilon}_2 = \bar{\varepsilon}_3, \bar{\varepsilon}_1 = 1.01$ as a function of $\bar{\varepsilon}_3$. (A colour version of this figure can be viewed online.)

$$W_{200}^{(2)} = -\frac{\mathrm{i}\bar{\varepsilon}_1\bar{\varepsilon}_2\bar{\varepsilon}_3^2\sqrt{\bar{\varepsilon}_1^2\bar{\varepsilon}_2^2}}{8008\sqrt{10}\pi\left(\log\left(-\frac{\mathrm{i}\bar{\varepsilon}_1}{\bar{\varepsilon}_2}\right)-\log\left(\frac{\mathrm{i}\bar{\varepsilon}_1}{\bar{\varepsilon}_2}\right)\right)}\times$$
$$\left(\bar{\varepsilon}_1^2\left(8\left(9\left(215\bar{\varepsilon}_2-462\right)\bar{\varepsilon}_3^2+90\left(56-43\bar{\varepsilon}_2\right)\bar{\varepsilon}_2\bar{\varepsilon}_3+\bar{\varepsilon}_2\left(8316\bar{\varepsilon}_2-18155\right)\right)+29640\bar{\varepsilon}_3+62215\right)\right.$$
$$+40\bar{\varepsilon}_1\left(72\left(14\bar{\varepsilon}_2^2-53\right)\bar{\varepsilon}_3-3631\bar{\varepsilon}_2^2+\left(9\bar{\varepsilon}_2\left(43\bar{\varepsilon}_2-224\right)+2890\right)\bar{\varepsilon}_3^2+7632\bar{\varepsilon}_2-2740\right)$$
$$\left.+40\left(741\bar{\varepsilon}_2^2-3816\bar{\varepsilon}_2+5480\right)\bar{\varepsilon}_3-2\left(8\bar{\varepsilon}_2\left(2079\bar{\varepsilon}_2-7225\right)+62215\right)\bar{\varepsilon}_3^2+5\bar{\varepsilon}_2\left(12443\bar{\varepsilon}_2-21920\right)\right), \tag{33}$$

Due to space limitations, explicit expressions for higher order are

$$W_{220}^{(2)} = -\frac{\mathrm{i}\bar{\varepsilon}_1\bar{\varepsilon}_2\bar{\varepsilon}_3^2\left(\bar{\varepsilon}_1-\bar{\varepsilon}_2\right)\sqrt{\bar{\varepsilon}_1^2\bar{\varepsilon}_2^2}}{16016\sqrt{15}\pi\left(\log\left(-\frac{\mathrm{i}\bar{\varepsilon}_1}{\bar{\varepsilon}_2}\right)-\log\left(\frac{\mathrm{i}\bar{\varepsilon}_1}{\bar{\varepsilon}_2}\right)\right)}\times$$
$$\left(8\bar{\varepsilon}_3^2\left(27\bar{\varepsilon}_1\left(215\bar{\varepsilon}_2-462\right)-12474\bar{\varepsilon}_2+21860\right)-40\bar{\varepsilon}_3\left(\bar{\varepsilon}_1\left(3024\bar{\varepsilon}_2-6521\right)-6521\bar{\varepsilon}_2+11448\right)\right.$$
$$\left.+5\left(\bar{\varepsilon}_1\left(17192\bar{\varepsilon}_2-37329\right)-37329\bar{\varepsilon}_2+65760\right)\right). \tag{34}$$

not presented.

Fig. 2 shows the texture coefficient $W_{200}^{(n)}$ $(n = 1, \ldots, 4)$ for the strain state $\bar{\varepsilon}_2 = \bar{\varepsilon}_3, \bar{\varepsilon}_1 = 1.01$ as a function of $\bar{\varepsilon}_3$. The behavior of the texture coefficient $W_{220}^{(n)}$ $(n = 1, \ldots, 4)$ for the same deformation state is shown in Fig. 3. In both coefficients, it is shown that until ≈ 2% strains, first-order approximations are in perfect agreement with those of superior order, meanwhile second-order approximations

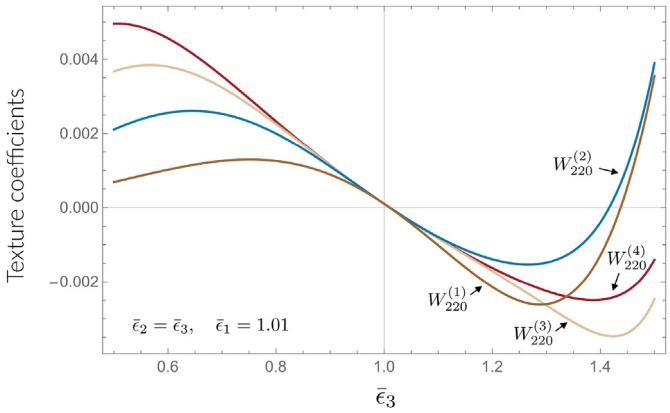

Fig. 3. Texture coefficient, $W_{220}^{(n)}$, of n-th order for the strain state $\bar{\varepsilon}_2 = \bar{\varepsilon}_3, \bar{\varepsilon}_1 = 1.01$ as a function of $\bar{\varepsilon}_3$. (A colour version of this figure can be viewed online.)

are in perfect agreement with those of superior order until ≈ 10% strains. Although we are interested in the linear part of the behavior, to be consistent with the second-order strain-induced volume changes affecting the effective volume fraction given by Eq. (7), our non-linear model includes second-order strain approximations for the texture. Therefore, $W_{200}^{(2)}$ and $W_{220}^{(2)}$ are selected all throughout the remainder of the document. However, note that after linearization —presented in next section—, any order texture solution derives in the same linearized piezoresistive coefficients.

3.2. Validating of the analytical procedure

In order to validate the previously introduced analytical formulation, effective conductivities given by

$$\boldsymbol{\sigma} = \boldsymbol{\sigma}_m + \langle f_0\left(\boldsymbol{\sigma}_f - \boldsymbol{\sigma}_m\right)\boldsymbol{A}\rangle, \tag{35}$$

are considered herein. The material properties in Table 1 have been used for the computations. Arbitrarily, the strain state $\bar{\varepsilon}_2 = \bar{\varepsilon}_3, \bar{\varepsilon}_1 = 1.01$ is set. Fig. 4 shows the dimensionless conductivities $\sigma_0/\sigma_{jj} - 1$ $(j = 1, 2$, no sum) as a function of $\bar{\varepsilon}_3$, being σ_0 the effective conductivity under no deformation. Second-order analytical predictions are compared to results obtained by García-Macías et al. [10] via numerical integration showing excellent agreement. Although not shown here, expression (29) for σ_{33} has been also

Table 1
Material parameters used in computations.

σ_m (Sm^{-1})	σ^L (Sm^{-1})	σ^T (Sm^{-1})	f_0	$S_{11} = S_{22}$	S_{33}
1.036×10^{-10}	3.5481×10^{2}	3.5481×10^{2}	0.01	0.499968	6.43526×10^{-5}

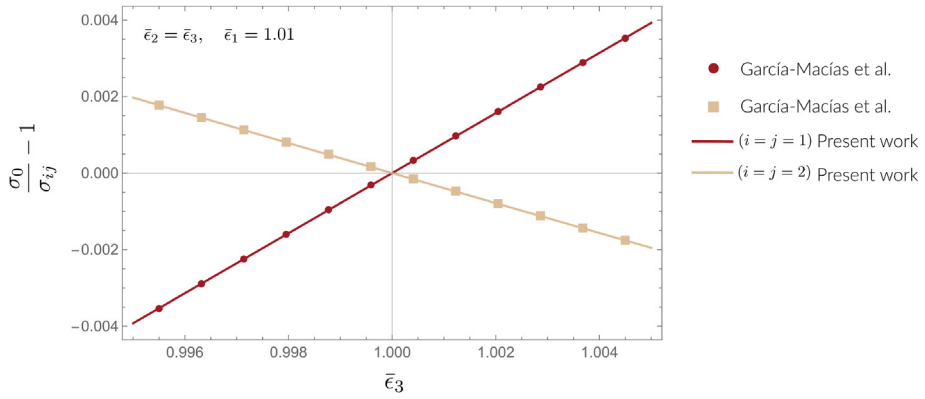

Fig. 4. Dimensionless conductivities for the strain state $\bar{\varepsilon}_2 = \bar{\varepsilon}_3, \bar{\varepsilon}_1 = 1.01$ as a function of $\bar{\varepsilon}_3$. Term σ_0 corresponds to the effective conductivity under no deformation. (A colour version of this figure can be viewed online.)

validated.

4. Formulas for linearized piezoresistivities

The relative electrical resistivity change is normally a non-linear function of the strain. Under the hypothesis of small deformations, these two quantities are linearly related as

$$\begin{pmatrix} \Delta\rho_{11}/\rho_0 \\ \Delta\rho_{22}/\rho_0 \\ \Delta\rho_{33}/\rho_0 \\ \Delta\rho_{23}/\rho_0 \\ \Delta\rho_{13}/\rho_0 \\ \Delta\rho_{12}/\rho_0 \end{pmatrix} = \begin{pmatrix} \lambda_{11} & \lambda_{12} & \lambda_{12} & 0 & 0 & 0 \\ \lambda_{12} & \lambda_{11} & \lambda_{12} & 0 & 0 & 0 \\ \lambda_{12} & \lambda_{12} & \lambda_{11} & 0 & 0 & 0 \\ 0 & 0 & 0 & \lambda_{44} & 0 & 0 \\ 0 & 0 & 0 & 0 & \lambda_{44} & 0 \\ 0 & 0 & 0 & 0 & 0 & \lambda_{44} \end{pmatrix} \begin{pmatrix} \varepsilon_{11} \\ \varepsilon_{22} \\ \varepsilon_{33} \\ 2\varepsilon_{23} \\ 2\varepsilon_{13} \\ 2\varepsilon_{12} \end{pmatrix}, \tag{36}$$

where ε_{ij} are the components of the small strain tensor, $\Delta\rho_{ij}$ are the changes in the components of the resistivity tensor $\boldsymbol{\rho} = \boldsymbol{\sigma}^{-1}$, and ρ_0 is the resistivity of the composite in the absence of strains. Six-dimensional matrix $\boldsymbol{\lambda}$ is known as the piezoresistivity of the composite which, by following previous works [10,27,57,58], it is in principle assumed to have a cubic symmetry with three independent components, that is λ_{11}, λ_{12} and λ_{44}.

This section introduces compact closed-form expressions for all the components of the piezoresistivity matrix in term of micromechanical parameters of the composite. To this end, we use the analytical model for conductivities in term of strains derived in the previous section. Then piezoresistivities are accomplished after a linearization procedure.

4.1. Composites without percolating network ($\xi = 0$)

We firstly consider the simpler case when no percolating networks are formed, that is $\xi = 0$, or, alternatively, the filler volume fraction is in the range $0 \leq f(\varepsilon) < f_c(\varepsilon)$. Then, only first and second terms remain in the model of equation (1). The methodology described in Section 3 provides us with an analytical solution for the conductivities —hence for piezoresistivities— in terms of the microstructural geometrical and material parameters, as well as the strain state. The three piezoresistivity coefficients can be obtained by two virtual experiments, namely a laterally constrained uni-axial stretching and a pure distortion. Note that after replacing the texture coefficients —Eqs. (33) and (34)— in Eqs. 27–29, effective conductivities are available for any arbitrary strain tensor since the texture coefficients and the volume fraction (7) are given in terms of the three (invariant) principal strains.

The first virtual experiment consists in a laterally constrained uni-axial stretching in x_n-direction, that is,

$$\varepsilon_1 = \varepsilon_n \text{ and } \varepsilon_2 = \varepsilon_3 = \varepsilon_t = 0. \tag{37}$$

In this case,

$$\frac{\Delta\rho_{nn}}{\rho_0} = \frac{\sigma_0}{\sigma_{nn}} - 1 = \lambda_n(\varepsilon_n), \tag{38}$$

and

$$\frac{\Delta\rho_{tt}}{\rho_0} = \frac{\sigma_0}{\sigma_{tt}} - 1 = \lambda_t(\varepsilon_n), \tag{39}$$

where t refers to a perpendicular direction to x_n-direction.

Introducing the strain state in Eq. (37) into Eqs. (33) and (34), and afterward in Eqs. (27) and (30), we arrive from (38) to the analytical non-linear function $\lambda_n(\varepsilon_n)$ that relates the change in the relative resistivity in the x_n-direction under a laterally constrained stretching in the x_n-direction. Following the same procedure but with equations (28) and (39), we obtain the non-linear function $\lambda_t(\varepsilon_n)$ that relates the change in the relative resistivity in the x_t-direction when a laterally constrained stretching in the x_n-direction takes place. For illustrative purposes, Figs. 5 and 6 show these two functions for a composite with the material parameters summarized in Table 1. Then, simple linearization of λ_n and λ_t at $\varepsilon_n = 0$ leads to

and

respectively, where

$$\lambda_{11} = \frac{f_0\left(5\mathcal{A}^2\sigma_{Tm}(S_{33}\sigma_{Lm} + \sigma_m) - 4\mathcal{A}\sigma_{Lm}\sigma_{Tm} + 2\mathcal{B}\sigma_{Lm}(\sigma_{Tm}(5\mathcal{B}S_{11} + 2) + 5\mathcal{B}\sigma_m)\right)}{5\sigma_{Lm}\sigma_{Tm}(\mathcal{A}f_0 + 2\mathcal{B}f_0 + 3)}, \tag{40}$$

$$\lambda_{12} = \frac{f_0\left(5\mathcal{A}^2\sigma_{Tm}(S_{33}\sigma_{Lm}+\sigma_m)+2\mathcal{A}\sigma_{Lm}\sigma_{Tm}+2\mathcal{B}\sigma_{Lm}(\sigma_{Tm}(5\mathcal{B}S_{11}-1)+5\mathcal{B}\sigma_m)\right)}{5\sigma_{Lm}\sigma_{Tm}(\mathcal{A}f_0+2\mathcal{B}f_0+3)}, \tag{41}$$

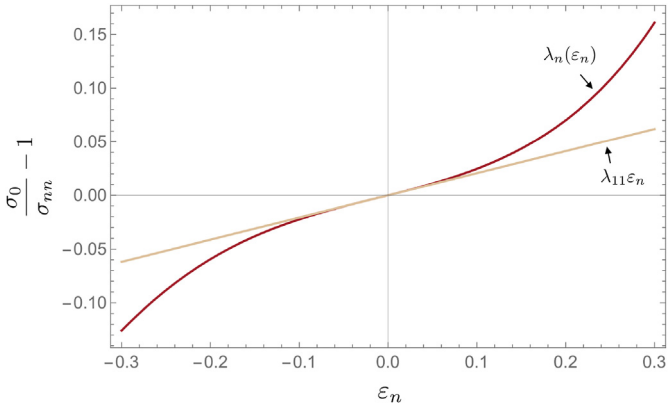

Fig. 5. Relative change in the resistivity in the x_n-direction as a function of ε_n for a composite material without percolating networks ($\xi = 0$). (A colour version of this figure can be viewed online.)

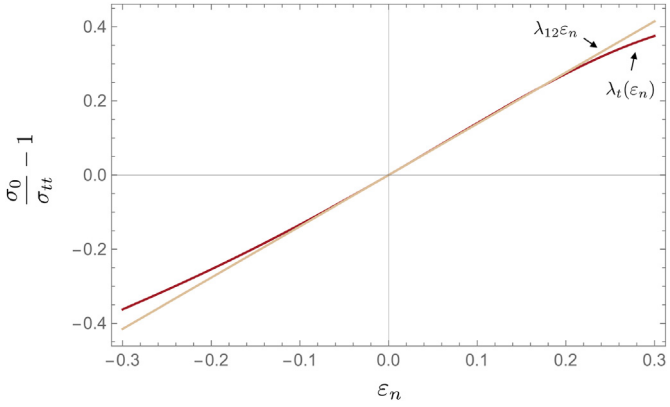

Fig. 6. Relative change in the resistivity in the x_t-direction (perpendicular to x_n-direction) as a function of ε_n for a composite material without percolating networks ($\xi = 0$). (A colour version of this figure can be viewed online.)

$$\mathcal{A} = \frac{\sigma_{Lm}}{(1-f_0)S_{33}\sigma_{Lm}+\sigma_m}, \tag{42}$$

$$\mathcal{B} = \frac{\sigma_{Tm}}{(1-f_0)S_{11}\sigma_{Tm}+\sigma_m}, \tag{43}$$

with $\sigma_{Lm} = \sigma^L - \sigma_m$ and $\sigma_{Tm} = \sigma^T - \sigma_m$. Note that any alternative uniaxial stretching deformation leads to the same results, showing that $\lambda_{11} = \lambda_{22} = \lambda_{33}$ and $\lambda_{12} = \lambda_{13} = \lambda_{23}$. Additionally, it also can be shown that $\lambda_{12} = \lambda_{21}$, $\lambda_{13} = \lambda_{31}$ and $\lambda_{23} = \lambda_{32}$, that is, piezoresistivity matrix $\boldsymbol{\lambda}$ —for this isotropic composite— is symmetric. This is not trivial since, unlike the elasticity tensor, there is no energetic arguments that guarantee such a symmetry.

In order to derive the third piezoresistive constant λ_{44}, a second experiment with a pure distortion is required. For instance,

$$\varepsilon_1 = -\varepsilon_{nt}, \varepsilon_2 = \varepsilon_{nt} \text{ and } \varepsilon_3 = 0. \tag{44}$$

Then,

$$\frac{\Delta\rho_{11}}{\rho_0} = \frac{\sigma_0}{\sigma_{11}} - 1 = \lambda_1(\varepsilon_{nt}), \tag{45}$$

and

$$\frac{\Delta\rho_{22}}{\rho_0} = \frac{\sigma_0}{\sigma_{22}} - 1 = \lambda_2(\varepsilon_{nt}), \tag{46}$$

where $\lambda_1(\varepsilon_{nt})$ and $\lambda_2(\varepsilon_{nt})$ can be obtained with the same procedure described above but now for the strains in Eq. (44). The change in the resistivity represented by these two functions corresponds to a principal system. But we need it in the system where the only non-zero strain is ε_{nt} in order to solve the system in Eq. (36). Taking into account the tensorial nature of the conductivities (as a second-order tensor not in the vectorial representation (36)), σ_{nt} can be computed after an appropriate coordinate transformation. After that, the relative change in the cross resistivity is obtained as

$$\frac{\Delta\rho_{nt}}{\rho_0} = \frac{\sigma_0}{\sigma_{nt}} - 1 = \lambda_{nt}(\varepsilon_{nt}). \tag{47}$$

Fig. 7 shows the evolution of λ_{nt} as a function of $2\varepsilon_{nt}$ along with its linearization at $\varepsilon_{nt} = 0$, which reads

$$\lambda_{44} = -\frac{3f_0(\mathcal{A}-\mathcal{B})}{5(\mathcal{A}f_0+2\mathcal{B}f_0+3)}. \tag{48}$$

Again, it can be shown that $\lambda_{44} = \lambda_{55} = \lambda_{66}$.

As a corollary of the results above, it is shown that the piezoresistive behavior of composites doped with randomly oriented fillers is indeed isotropic as the fulfillment

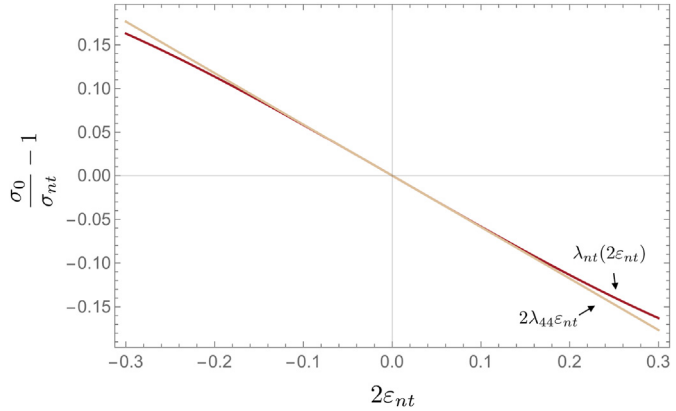

Fig. 7. Relative change in the cross resistivity (between x_t-direction and x_n-direction) as a function of the shear strain $2\varepsilon_{nt}$ for a composite material without percolating networks ($\xi = 0$). (A colour version of this figure can be viewed online.)

Table 2
Comparison of the analytical linear piezoresistivity coefficients and the numerical ones for a composite material without percolating networks ($\xi = 0$).

	λ_{11}	λ_{12}
Compression (García-Macías et al. [10])	0.192052	1.326842
Tension (García-Macías et al. [10])	0.206883	1.430713
Present work	0.206586	1.383820

$$\lambda_{44} = \frac{\lambda_{11} - \lambda_{12}}{2} \tag{49}$$

can be proven from Eqs. (40), (41) and (48). Therefore, there is no need to use the pure distortion virtual experiment in Eq. (44), being possible to achieve a complete description of the piezoresistive behavior of the composite in Eq. (36) using one single uni-axial stretching test like the one in Eq. (37).

Table 2 presents a comparison of the estimates of λ_{11} and λ_{12} with the results obtained with the numerical algorithm proposed by García-Macías et al. [10], showing very good agreements.

4.2. Composites with percolating networks ($\xi > 0$)

In this section, we consider composites with percolating networks of fibres by adding the third term in equation (1). The challenge in this model is that the effect of the reorientation of the fibres induced by external deformations modifies the percolation threshold f_c. Consequently, the parameter ξ in (1) also depends on the strains because both $f(\varepsilon)$ and $f_c(\varepsilon)$ are also functions of the strains as shown in Eqs. (7) and (2).

In order to account for this dependency of the strains in the percolation threshold, we follow the idea by García-Macías and co-authors [10], who exploited the strain-dependency of the ODF in Eq. (8) within the percolation theory set out by Komori and Makishima [33]. According to the reformulation developed by Kumar and Rawal [59], the percolation threshold for rod-like fiber-reinforced composites can be estimated as:

$$f_c(\varepsilon_n) = \frac{\pi}{5.77 s I(\varepsilon_n)}, \tag{50}$$

being

$$I = \int_0^{\pi}\int_0^{\pi} J(\theta,\psi)\hat{w}(\theta,\psi)\sin\theta \mathrm{d}\theta\mathrm{d}\psi, \tag{51}$$

with

$$J(\theta,\psi) = \int_0^{\pi}\int_0^{\pi} \sin\tau(\theta,\theta',\psi,\psi')\hat{w}(\theta',\psi')\sin\theta' \mathrm{d}\theta'\mathrm{d}\psi', \tag{52}$$

and

$$\sin\tau = \left[1 - (\cos\theta\cos\theta' + \cos(\psi-\psi')\sin\theta\sin\theta')^2\right]^{1/2}. \tag{53}$$

Note that the strain-dependency is introduced in Eq. (50) through the ODF $\hat{w}$, which is the same fiber ODF w previously introduced in Section 3, but normalized such that

$$\int_0^{\pi}\int_0^{\pi} \hat{w}(\theta,\psi)\sin\theta \mathrm{d}\theta\mathrm{d}\psi = 1. \tag{54}$$

In this work, the inverse of the $I(\varepsilon_n)$ is approximated for a simple stretching (ε_n) as a linear combination of a log(•) function and a linear function as follows:

$$I^{-1}(\varepsilon_n) = 1.27327 + 0.25457\varepsilon_n - 0.25461 log(\varepsilon_n + 1). \tag{55}$$

Fig. 8 shows the percolation threshold function f_c (Eq. (50)) for a fiber with aspect ratio $s = 100$ obtained by numerical integration of I (denoted with scatter points), and with the solution (55) for I (denoted with solid line), showing an excellent agreement for a wide range of deformations.

Following the same previous virtual experiment consisting in a laterally constrained uni-axial stretching in x_n-direction, i.e.

$$\varepsilon_1 = \varepsilon_n \text{ and } \varepsilon_2 = \varepsilon_3 = \varepsilon_t = 0, \tag{56}$$

the two functions $\lambda_n(\varepsilon_n)$ and $\lambda_t(\varepsilon_n)$ for relative changes in resistivity can be computed via analytical solution of the conductivity considering now the complete solution in Eq. (1), i.e., by adding the third percolating term. In this case, ξ in equation (2) is evaluated with the percolation threshold by the Komori-Makishima model in Eq. (50) through the proposed analytical interpolation in Eq. (55). Figs. 9 and 10 show these two functions for a composite with the material parameters summarized in Table 1. Recall that, in order to

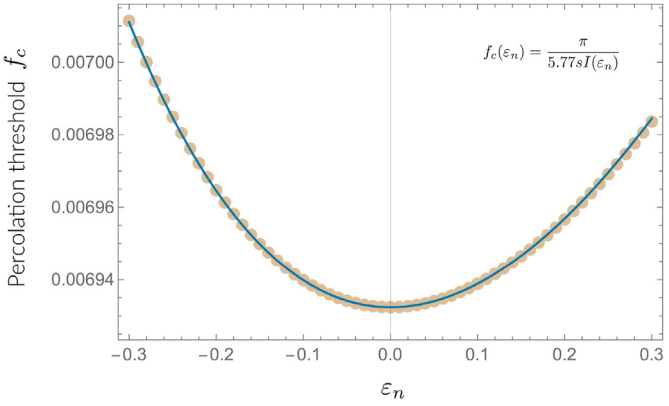

Fig. 8. Percolation threshold as a function of strain ε_n for a fiber-reinforced composites with filler aspect ratio $s = 100$. Points correspond to the solution obtained by the numerical integration of I while the solid line corresponds to the analytical interpolation solution of I. (A colour version of this figure can be viewed online.)

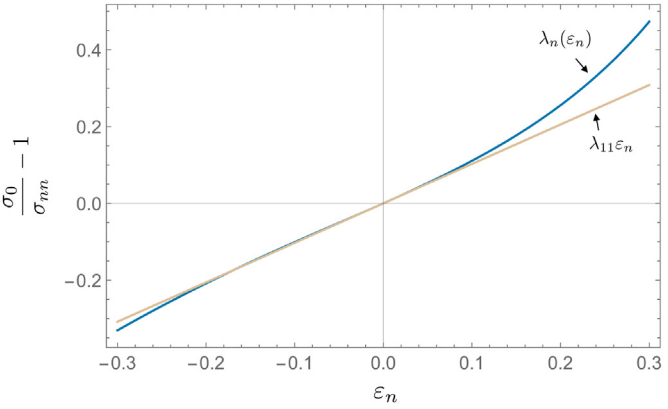

Fig. 9. Relative change in the resistivity in the x_n-direction as a function of ε_n for a composite material with percolating networks ($\xi > 0$). (A colour version of this figure can be viewed online.)

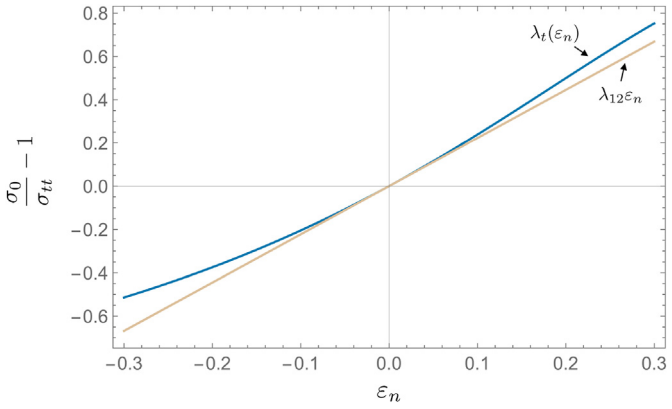

Fig. 10. Relative change in the resistivity in the x_t-direction (perpendicular to x_n-direction) as a function of ε_n for a composite material with percolating networks ($\xi > 0$). (A colour version of this figure can be viewed online.)

Table 3
Comparison of the analytical linear piezoresistivity coefficients and the numerical ones for a composite material with percolating networks ($\xi > 0$).

	λ_{11}	λ_{12}
Compression (García-Macías et al. [10])	0.99785	2.14837
Tension (García-Macías et al. [10])	1.07622	2.32250
Present work	1.02751	2.22751

model conductive networks, the Eshelby's tensor for the percolating term $\boldsymbol{A}_P$ is always set for infinite long fibers. Therefore, after the proper limiting process in (5), the Eshelby's components become $S_{11} = S_{22} = 1/2$ and $S_{33} = 0$. Moreover, for this example, the conductivity tensor is set equal for both the percolating ($\boldsymbol{\sigma}_P$) and the non-percolating ($\boldsymbol{\sigma}_{NP}$) mechanisms. Nevertheless, this is not necessary for our formulation as shown in the last section.

Then, from linearization of λ_n and λ_t at $\varepsilon_n = 0$, we arrive to closed-form formulas for the piezoresistivity coefficients λ_{11} and λ_{12}, which account for the percolation mechanism. Although they remain still quite simple, these expressions —and the non-percolating counterpart (Eq. (40) and (41))— are presented in Supplementary Material 1 due to space constraints. Additionally, Matlab [60] and Python [61] codes are also provided as Supplementary Material 2 with both solutions.

Table 3 presents a comparison of the analytical estimates of the piezoresistivity coefficients λ_{11} and λ_{12} and the numerical counterparts following the approach by García-Macías et al. [10], showing once again very good agreement.

4.3. Onset of the percolation phenomenon

The conductivity model in Eq. (1) —and hence the piezoresistivity model— is a piecewise function depending if the percolation phenomenon takes place or not, or alternatively, if fillers can touch each other forming micro-scale electrically conductive paths or not. This switch on-off percolation interplay is taken into account through parameter, ξ, i.e. the fraction of percolated fibres. According to Eq. (2), percolation occurs when $\xi > 0$. Parameter ξ can be modeled as a piecewise function as reported in Eq. (2). Thus, considering a simple stretching deformation state, ξ depends on the strain, ε_n, and the aspect ratio of the fiber, s. When there is no deformation, there exists a critical volume fraction f_0^* for which composites doped with filler volume fractions (f_0) below this critical value never percolate. This critical value is nothing else but the percolation threshold for $\varepsilon_n = 0$, that is

$$f_0^* = f_c(0) = \frac{0.693257}{s}, \tag{57}$$

and then $\xi > 0$ for $f_0 > f_0^*$. Specifically, the piecewise functional relationship between ξ and f_0 and s when $\varepsilon_n = 0$ is given by

$$\xi(f_0, s) = \begin{cases} 0, & 0 \le f_0 \le f_0^* \\ \dfrac{(f_0)^{1/3} - 0.885044(s)^{-1/3}}{1 - 0.885044(s)^{-1/3}}, & f_0 > f_0^*. \end{cases} \tag{58}$$

Fig. 11 (a) qualitatively shows the functional relationship (58) between ξ and f_0 (for a given aspect ratio s); together with the critical value f_0^* and an arbitrary unstrained volume fraction, $f_0^1 > f_0^*$. Fig. 11 (b) shows that fibers with a given aspect ratio s and with a

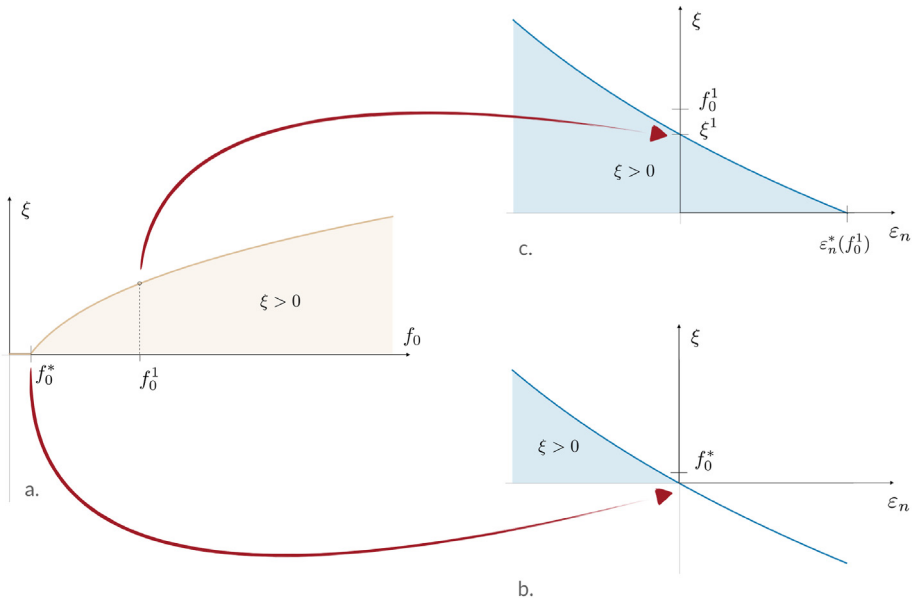

Fig. 11. Qualitative schema of (a) the $\xi(f_0)$ function when $\varepsilon_n = 0$; (b) the $\xi(\varepsilon_n)$ function when $f_0 = f_0^*$; and (c) the $\xi(\varepsilon_n)$ function when $f_0 = f_0^1$. (A colour version of this figure can be viewed online.)

volume fraction f_0^* could percolate for compression strains, but not for tension, resulting in discontinuous piezoresistivity coefficients at that point. The same kind of fiber with a volume fraction like f_0^1 is in percolation for a range of positive strains as sketched in Fig. 11 (c). However, for a critical value of the strain, $\varepsilon_n^*(f_0)$, eventually the percolation mechanism disappears. In any case, it is pictured that the fraction of percolated fibres decreases with ε_n.

In order to illustrate the shift in the piezoresistivity coefficients at the percolation threshold f_0^*, Fig. 12 shows the piezoresistivity coefficients λ_{11} and λ_{12} as a piecewise function of the unstrained volume fraction f_0 for the same composite of Section 4.2. It is noted that the strain-sensitivity of the composite monotonically increases as the volume fraction approaches the unstrained percolation threshold, where maximum piezoresistivity coefficients are found. Beyond f_0^*, the piezoresistivity coefficients monotonically decrease until reaching an stable value.

5. Application to strain-sensing carbon nanotube composites

In this last section, the potentials of the derived analytical formulation are illustrated with its application to the modeling CNT-based composites. The use of CNTs as nanoscale inclusions has engaged growing interest in recent years due to their vast potential for the development of multifunctional and smart materials. Many research works have reported the exceptional physical properties of CNTs, including elastic moduli greater than 1 TPa and ultimate tensile strengths around 150 GPa, electrical conductivities between 1000 and 200000 S/cm, high aspect ratio ($\approx$100–1000), lightness and excellent thermochemical stability [62].

We center our attention on the implementation of the micromechanics modeling of the electrical conductivity and the piezoresistive behavior of CNT-based composites previously proposed in Refs. [13,19,20,27] to the newly proposed analytical approach above. Such a model distinguishes two different mechanisms governing the electrical conductivity of these composites, namely the electron hopping and the conductive networking mechanisms. The electron hopping mechanism relates a quantum tunneling effect through which electrons can migrate between proximate non-connected fillers. Such an effect dominates the electrical conductivity of the composite at low CNT concentrations. With increasing filler loadings (above the percolation threshold), the separation among the tubes decreases until adjacent fibers touch one another forming microscale conductive paths. Note that the contributions

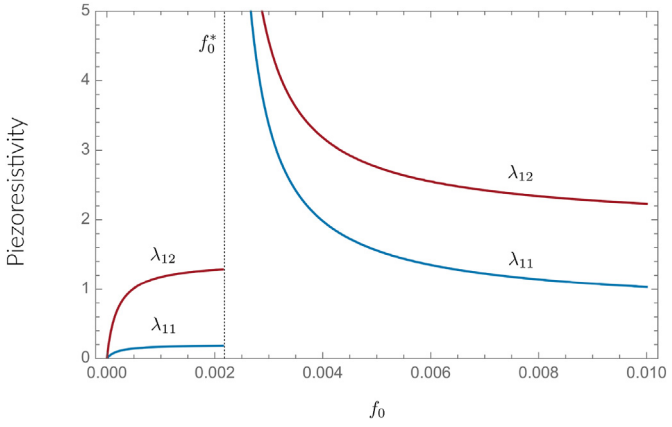

Fig. 12. Piezoresistivities coefficients, λ_{11} and λ_{12} as a function of the unstrained volume fraction f_0. A sudden shift is observed at percolation threshold f_0^*. (A colour version of this figure can be viewed online.)

Table 4
Material parameters used for the modeling of CNT/epoxy composites.

Mass of electron (m)	$9.10938291 \times 10^{-31}$ kg
Electric charge of an electron (e)	$-1.602176565 \times 10^{-19}$ C
Reduced Planck's constant ($\hbar$)	6.626068×10^{-34}m^{2}kg/s
Electrical conductivity of epoxy (σ_m)	1.036000×10^{-10} S/m
Electrical conductivity of CNTs ($\sigma^L = \sigma^T = \sigma_c$)	10^2–10^7 S/m
Length of CNTs	3.27 μm
Diameter of CNTs	10.15 nm
Strain range	−5/5%
Mass density of CNTs (ρ_c)	1.39 g/cm^3
Mass density of epoxy (ρ_m)	1.12 g/cm^3
Height of the potential barrier (λ)	0.5 eV
Cut-off inter-particle distance (d_c)	1.87 nm

of the electron hopping and the conductive networking mechanisms describe the percolating and non-percolating phases in the MT's model in Eq. (1). Therefore, CNT-based polymer composites fall within the scope of the proposed analytical approach.

A concise description of the micromechanics modeling of CNT-based composites is presented in Appendix 7, although interested readers may find further details in Refs. [13,19,20,27]. Computer codes in MATLAB [60] and Python [61] languages with the implementation of the micromechanics model in the developed analytical approach are also provided in the Supplementary Material 2. It is important to remark that, although CNTs present substantially larger aspect ratios than other conductive fillers such as e.g. carbon fibers, the schematic RVE representation in Fig. 1 remains theoretically correct. This is due to the fact that the geometry of the fillers is encapsulated in the Eshelby's tensor **S**, and no fundamental modifications need to be addressed in the theoretical formulation from Eq. (1). Another topological aspect of CNTs that does require especial consideration concerns the circumstance that CNTs usually acquire certain degree of waviness during mixing because of their low bending stiffness (see Fig. 18 in Appendix A). Nevertheless, as reported by Feng and Jiang [26] and García-Macías et al. [19], filler waviness can be readily introduced in the presented micromechanics approach through equivalent straight fillers with waviness-dependent aspect ratio and volume fraction. The incorporation of waviness effects does not alter the structure of the presented solutions, so specific results and discussion are omitted hereafter for simplicity. Nonetheless, interested readers can find further details in Appendix A.

The material parameters used in the subsequent numerical results are collected in Table 4, and taken from the author's experience and literature data for CNT/epoxy composites. Filler contents are typically reported in practice in terms of mass content *wt*, which may be related to the filler volume fraction by the following relation:

$$f = \frac{\rho_m\, wt}{\rho_m\, wt + (1 - wt)\rho_c}, \tag{59}$$

with ρ_m and ρ_c being the mass densities of the matrix phase and the CNTs given in Table 4, respectively.

Fig. 13 shows the analytical estimates of the effective electrical conductivity of CNT/based composites considering different electrical conductivities of CNTs σ_c. Additionally, the analytical results obtained without considering the contribution of the conductive networks mechanism (i.e. $\xi = 0$) are also depicted with dashed lines for illustrative purposes. It is clearly noted in this figure that, after percolation, the effective electrical conductivity of the composite is majorly dominated by the conductive networking mechanism.

The effect of strain upon the contribution of the conductive networking mechanism is investigated in Fig. 14 for an epoxy/CNT

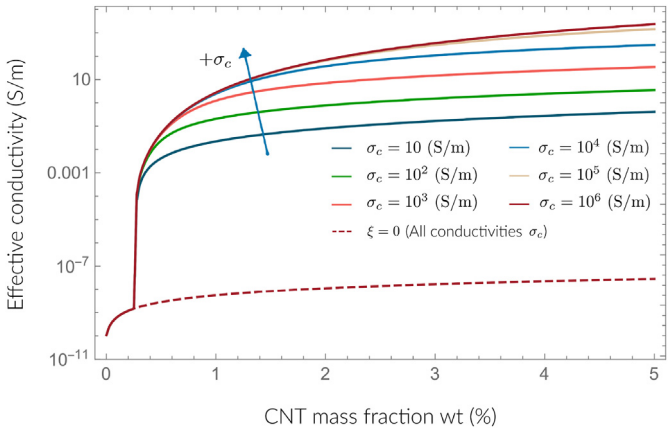

Fig. 13. Effective electrical conductivity of CNT/epoxy composites for varying electrical conductivities of the CNTs σ_c. (A colour version of this figure can be viewed online.)

composite doped with 1% CNT mass content. Fig. 14 (a) shows the relative variation of the percolation threshold f_c using the analytical interpolation approach presented in Section 4.2 for laterally constrained uni-axial strain conditions. It is noted in this figure that either compression or tension strains lead to increasing percolation threshold as a result of the strain-induced loss of randomness in the nanofillers orientation distribution. On the other hand, Fig. 14 (b) depicts the variation of the fraction of percolated CNTs ξ as a function of the applied strain under laterally constrained conditions. It is observed in this figure that the amount of percolated CNTs decreases with increasing strain under tensile strains. In this case, the strain-induced increase of the percolation thresholds adds up with the breakage of electrically conductive paths as a result of the volume expansion. Conversely, under compressive strains, these two mechanisms generate opposite effects [27]. Although the percolation threshold increases with higher compressive strains, the increase of the effective filler volume fraction dominates the small range of deformation and, therefore, increasing compression implies larger numbers of conductive paths.

The results of the modeling of the piezoresistive behavior of CNT/epoxy composites are reported in Figs. 15 and 16. Fig. 15 shows the relative change in resistivity in the x_n-direction (a) and in the x_t-direction (b) of CNT/epoxy composites subjected to a laterally constrained uni-axial stretching virtual test. In this figure, the role exerted by the considered piezoresistive mechanisms can be comprehended. Firstly, it is clear that the conductivity of the composite increases for increasing compressive strains, while the opposite behavior is found for tensile strains. This behaviour is ascribed to the strain-induced volume expansion effects, which becomes dominant for CNT-based composites. Although the percolation threshold increases (i.e. the breakage of conductive paths takes place) both under compression and tension as shown in Fig. 14 (a), the effect of the volume expansion becomes predominant for the considered range of deformation. Indeed, only some slight differences can be observed for compression and stretching strains. After a closer inspection of the results and the analysis of the piezoresistivity coefficients reported below, it is concluded that the strain sensitivity under tensile strains is slightly higher than under compression strains. These differences, which have been also observed previously in experiments (see e.g. Ref. [63]), are justified by the different signs of the considered strain-induced effects under tension and compression. Note that, when the composite is subjected to stretching, both the volume expansion and filler reorientation decrease the overall electrical conductivity of the composite. Conversely, when compression takes place, the volume expansion (the dominant mechanism) tends to increase the electrical conductivity while the filler reorientation induces the opposite effect, with the subsequent smaller strain sensitivity. For a detailed analysis and further discussion of the roles played by the considered mechanisms upon the electrical conductivity of CNT-based composites, readers are referred to Ref. [27]. Finally, in order to characterize the piezoresistivity coefficients, and given the difficulties involved in obtaining compact expressions in this particular case study, a least squares linear regression is adjusted in the strain range leading to a coefficient of determination of 0.9999 likewise references [10,27]. Then, the piezoresistivity coefficients λ_{11} and λ_{12} are computed as the slope of the regression of their corresponding strain-sensitivity curves. The piezoresistivity

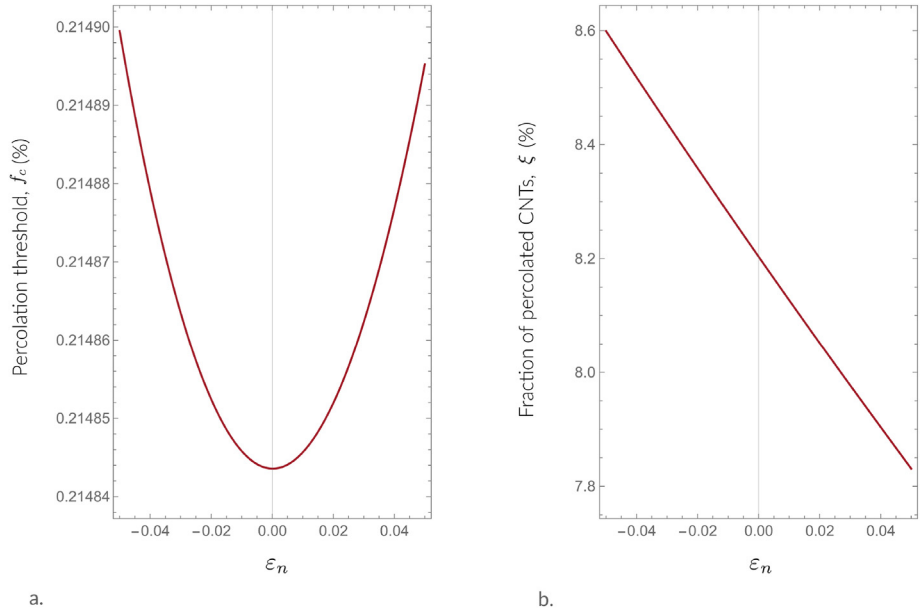

Fig. 14. Variation of the percolation threshold f_c (a) and the normalized percentage of percolated CNTs ξ (b) with respect to the strain level under laterally constrained conditions (1% CNT wt). (A colour version of this figure can be viewed online.)

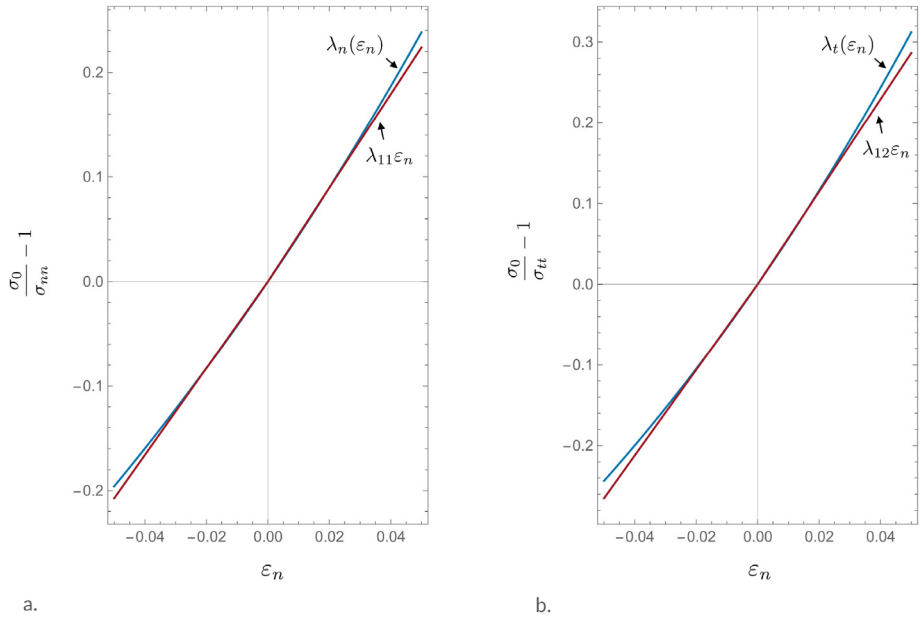

Fig. 15. Relative change in the resistivity in the x_n-direction (a) and in the x_t-direction (b) as a function of ε_n for a CNT/epoxy composite loaded with 1% CNT wt. (A colour version of this figure can be viewed online.)

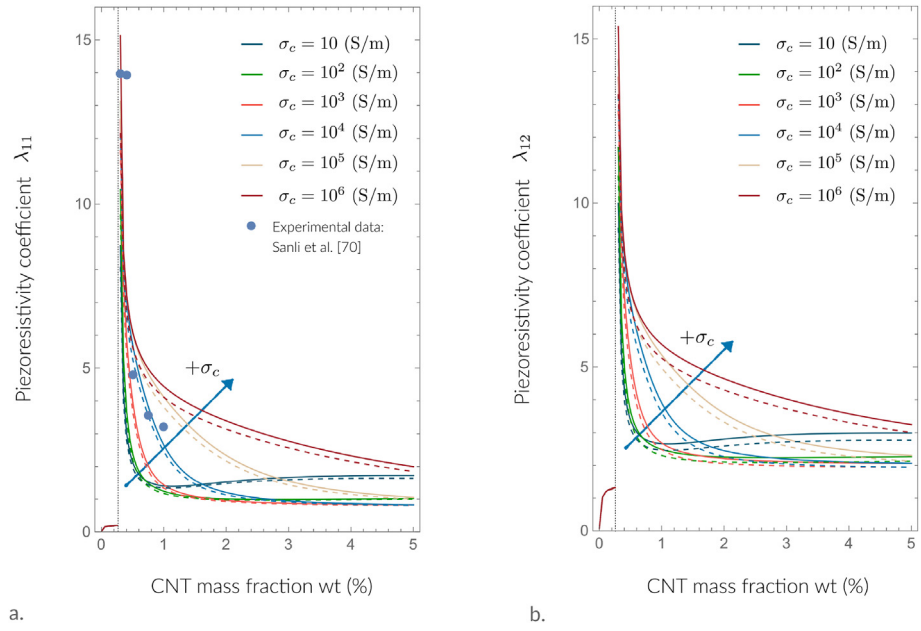

Fig. 16. Piezoresistivity coefficients of CNT/epoxy composites versus filler mass concentration under laterally constrained uni-axial compression/stretching for different filler conductivities σ_c. Solid and dashed lines stand for piezoresistivity coefficients computed for tension and compression strains. (A colour version of this figure can be viewed online.)

coefficients are computed by fitting separately the electrical resistance variations under compression and traction strains.

Following the previous analysis for filler mass contents ranging between 0 and 5%, Figs. 16 (a) and (b) depict the piezoresistivity coefficients λ_{11} and λ_{12} as functions of the filler concentration, respectively. Theoretical predictions in Fig. 16 (a) are compared against experimental data reported by Sanli and co-authors in Ref. [70] for epoxy/MWCNT composites. Note that those authors investigated the piezoresistive properties of standard dog-bone samples, where the longitudinal piezoresistive behaviour λ_{11} is assessed. The comparison demonstrates the proposed approach is capable to reproduce the decreasing tendency of λ_{11} after the percolation threshold, with close theoretical/experimental agreements when considering the electrical conductivity of CNTs as $\sigma_c = 10^4$ Sm^{-1}. In these figures, the piezoresistivity coefficients computed under tension and compression strains are depicted with solid and dashed lines, respectively. As anticipated above, the piezoresistivity coefficients considering tensile strains are slightly than those obtained for compression strains. Nonetheless, such differences are small enough that a common piezoresisitvity coefficient can be assumed, for instance the mean value. It is also noticeable that more conductive fillers generally lead to larger piezoresistivity coefficients. It is also noted that, alike the results previously reported in Fig. 12, the piezoresistivity coefficients reach maximum

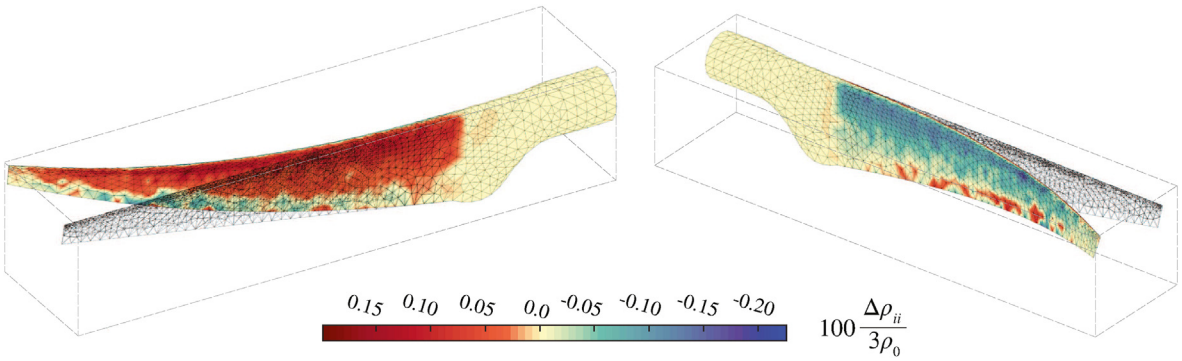

Fig. 17. Contour plot of the hydrostatic part of the relative change in the electrical resistivity tensor in a toy example of a solid 3D wind turbine blade made of CNT/epoxy composite ($\sigma_c = 10^4$ S/m, 1 wt%). (A colour version of this figure can be viewed online.)

values at the percolation threshold. In addition, the transverse piezoresistivity coefficient λ_{12} also exhibits here larger values compared to the longitudinal coefficient λ_{11} along the whole range of filler concentrations. This behavior finds an explanation in the reorientation effect. For instance, in the case of tensile strains, fillers tend to align in the direction of the strain and, thus, the longitudinal resistivity experiences comparatively smaller reductions. Nevertheless, a closer inspection reveals that λ_{11} and λ_{12} have similar orders of magnitude for all the consider filler contents, being the shear piezoresistivity coefficient λ_{44} around two orders or magnitude smaller according to Eq. (49). This evidence supports the extended conception of CNT-based composites as volumetric strain sensors, being possible to obtain reasonable approximations accounting for one single piezoresistivity coefficient, i.e. $\lambda_{11} \approx \lambda_{12}$ and $\lambda_{44} = 0$. Hence, a reasonable approximation may be to consider $\lambda_{11} = \lambda_{12} = \lambda$, with λ being the average value of the analytical piezoresistivity coefficients reported in Eqs. (SM3) and (SM4) in the Supplementary Material 1. Under such an approximation, the eletromechanical relation in Eq. (36) for the spherical part is:

$$\frac{\Delta\rho_{ii}}{3\rho_o} = \frac{\lambda_{11} + 2\lambda_{12}}{3}\varepsilon_{ii} \approx \lambda\varepsilon_{ii}. \tag{60}$$

Finally, in order to demonstrate the potential of the developed analytical approach for the modeling of 3D macroscopic structural elements, it has been inserted into a standard solid FEM code developed in MATLAB environment. In particular, as a toy example of a geometrically complex structure requiring a considerable mesh density, a solid wind turbine blade has been modeled. The wind turbine blade is approximately 50 cm long and has a variable width ranging from 10 cm to 3 cm, with a solid cylindrical axis with a diameter of 6 cm, and an aerodynamic curved blade. The FEM code incorporates the micromechanics model of CNT-based composites implemented in the analytical approach presented in Section 3 and provided in the Supplementary Material 2. The blade has been meshed with four-nodes linear tetrahedral elements with 0.9 cm long edges on average. The discretization amounts to 2248 nodes and 7833 elements. The material properties of the blade has been defined according to the parameters reported in Table 4 with CNT electrical conductivities of $\sigma_c = 10^4$ S/m and dispersed at a mass concentration of 1 wt%. The mechanical properties of the material are assumed elastic isotropic with a Young's modulus of 3.0 GPa and a Poisson's ratio of 0.3. The blade has been simulated considering fixed boundary conditions at the external face of the axis, and a static imposed displacement of 2.5 cm along the transverse direction of the blade. The code extracts the hydrostatic part of the tensor of relative variations of the electrical conductivity of the material at every Gauss integration point according to Eq. (60) as shown in the contour plot in Fig. 17. The determination of the strain-induced effects upon the conductivity is completely analytical according to Section 3 except for the determination of the percolation threshold, which has been computed by direct numerical integration of the Komori-Makishima model in Eq. (50) using the Simpson's rule. Nevertheless, given the similarity between λ_{11} and λ_{12} reported above, the same simulation using the approximation from Eq. (60) reports very similar results, achieving maximum relative errors below 0.9% with extremely low computational burden.

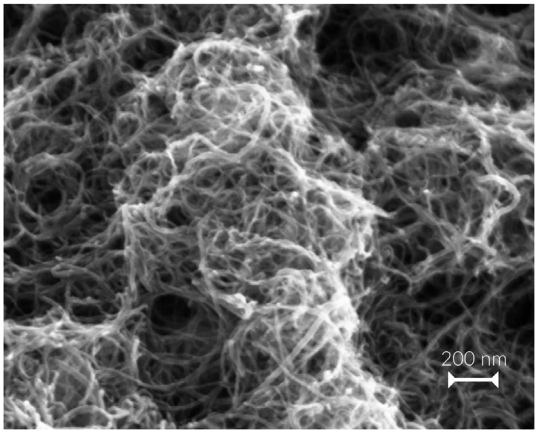

Fig. 18. SEM picture of MWCNTs in aqueous suspension after mechanical mixing.

6. Conclusions

In this work, an analytical micromechanics approach for the modeling of the electrical conductivity and piezoresistivity of short-fiber reinforced composites with percolation-type behavior has been presented. The formulation accounts for two distinct mechanisms, percolating and non-percolating phases, that contribute to the overall conductivity of the composites. These two mechanisms are included in a multi-inclusion expansion of the MT model, and the effects of external mechanical strains are included by means of three different phenomena: (*i*) volume expansion; (*ii*) filler reorientation; and (*iii*) variation of the percolation threshold. Second-order closed-form solutions of the strain-dependent effective electrical conductivity and the linear piezoresistivity coefficients have been derived by means of generalized spherical harmonics series expansions of the MT model. The presented theoretical derivations have demonstrated that, under the

assumptions of small strains and inextensible fibers, the piezoresistivity matrix of randomly oriented short-fiber composites is symmetric and it presents isotropic behavior. As a consequence, it has been proved that one single stretching test suffices to fully characterize all the piezoresistivity coefficients. The derived formulas are available in MATLAB and Python languages as part of the supplementary material as a tool for free use of the community.

The proposed formulation has been applied to the modeling of composites doped with CNTs, incorporating the electron hopping or quantum tunneling mechanism and the formation of electrically conductive microscopic conductive paths as non-percolating and percolating phases, respectively. Numerical results and discussion have been presented to demonstrate the accuracy of the proposed formulation, and an illustrative toy example of the electromechanical modeling of a 3D CNT/epoxy macroscopic structure has been reported. The numerical results evidence the computational efficiency of the proposed approach, being possible to link the electromechanical response of macroscopic structural systems with the microstructural properties of the composites. It is important to remark that the presented formulation is suitable for short-fibers or any other doping filler conceivable as inclusions with prolate geometry and transversely isotropic conductivity. Nonetheless, the formulation can be also extended to other types of inclusions by adequately modifying the Eshelby's tensor in Eq. (4). For instance, the expression of the Eshelby's tensor for oblate inclusions could be incorporated to model graphene nanoplatelet (or graphene nanosheet) fillers. Overall, the presented formulation is envisaged to offer vast potentials for the analysis of macroscopic response of short-fiber reinforced composite structures, including among others the consideration of heterogeneous dispersions of fillers, functionally graded materials, material optimization, and uncertainty propagation analyses.

CRediT authorship contribution statement

Federico C. Buroni: Conceptualization, Methodology, Formal analysis, Investigation, Software (Section 3 and 4), Visualization, Writing – original draft, Writing – review & editing, Project administration, Funding acquisition. **Enrique García-Macías:** Methodology, Investigation, Software (Section 5 and Supplementary Material 2), Validation, Visualization, Data curation, Resources, Writing – original draft, Writing – review & editing.

Declaration of competing interest

The authors declare that they have no known competing financial interests or personal relationships that could have appeared to influence the work reported in this paper.

Acknowledgments

This work was supported by the Ministerio de Economía y Competitividad through the research project DPI2017-89162-R and by the Consejería de Economía, Conocimiento, Empresas y Universidad de la Junta de Andalucía (Spain) through the research project P18-RT-3128. Both projects were co-funded by the Fondo Europeo de Desarrollo Regional (FEDER), Programa Operativo FEDER 2014–2020.

Appendix A. Summary of the CNT-nanocomposite model

The micromechanics modeling of the electrical conductivity of CNT-based composites previously developed in Refs. [13,19,20,27] and used in Section 5 is concisely overviewed herein. Two different mechanisms have been recognized to govern the electrical conductivity of these composites, namely electron hopping and conductive networking. The electron hopping mechanism is characterized by a quantum tunneling effect through which electrons can migrate between proximate non-connected fillers. Such an effect governs the electrical conductivity of the composite at low CNT concentrations. With increasing CNT concentration, the separation distance among CNTs decreases until adjacent fibers touch one another resulting in a continuous electrically microscale conductive path.

For the sake of clarity in the subsequent derivations, subscript χ is used to relate the corresponding magnitudes to the electron hopping (EH) and the conductive networking (CN) mechanisms. Recall that, as previously indicated in Section 2, the quantities associated with the electron hopping (non-percolating) mechanism are defined with the real fillers aspect ratio, while quantities corresponding to conductive networking (percolating) mechanism are defined with an infinite aspect ratio ($s \to \infty$).

The probability of occurrence of the electron hopping mechanism is highly dependent on the distance between tubes. The average separation distance $d_a(\varepsilon)$ between adjacent CNTs has been reported to follow a power-law description [13]:

$$d_{a,\chi}(\varepsilon) = \begin{cases} d_c & \chi = EH \\ d_c \left(\dfrac{f_c(\varepsilon)}{f(\varepsilon)} \right)^{1/3} & \chi = CN \end{cases} \tag{61}$$

with d_c being the maximum possible separation between two CNTs that permits the tunneling penetration of electrons, often termed the cut-off distance. A value of $d_c = 1.8$ nm in chosen in most polymer matrix materials [64]. This effect can be simulated by means of a continuum interphase layer surrounding the nanotubes. The electrical contact resistance of the interfaces of the CNTs can be estimated by the generalized Simmons formula [24] as follows:

$$R_{int,\chi}\left(\varepsilon, d_{a,\chi}(\varepsilon)\right) = \frac{d_{a,\chi}(\varepsilon)\hbar^2}{ae^2(2\ m\lambda)^{1/2}} \exp\left[\frac{4\pi d_{a,\chi}(\varepsilon)}{\hbar}(2\ m\lambda)^{1/2}\right], \tag{62}$$

where m and e are the mass and the electric charge of an electron, respectively, λ is the height of the tunneling potential barrier (taken as 5.0 eV as a common value for polymer composites [13]), a is the contact area of the CNTs and $\hbar$ stands for the reduced Planck's constant. Hence, the conducting inter-phases around the CNTs can be defined with a thickness t and an electrical conductivity σ_{int} given by Ref. [65]:

$$t_\chi = \frac{1}{2} d_{a,\chi}(\varepsilon), \quad \sigma_{int,\chi} = \frac{d_{a,\chi}(\varepsilon)}{aR_{int,\chi}\left(\varepsilon, d_{a,\chi}(\varepsilon)\right)} \tag{63}$$

The interphase layer is often accounted for by an effective composite solid cylinder model. The conductivity tensor of the equivalent solid cylinder, $\boldsymbol{\sigma}_c$, is defined as transversely isotropic in the local coordinate system with effective longitudinal $\tilde{\sigma}^L$ and transverse $\tilde{\sigma}^T$ electrical conductivities. By applying Maxwell's equations and the law-of-mixture rule, $\tilde{\sigma}^L$ and $\tilde{\sigma}^T$ can be written as [13]:

$$\tilde{\sigma}_{\chi}^{L}(\varepsilon)=\frac{(L+2t_{\chi}(\varepsilon))\sigma_{int,\chi}(\varepsilon)\left[\sigma_{c}^{L}r_{c}^{2}+\sigma_{int,\chi}(\varepsilon)\left(2r_{c}t_{\chi}(\varepsilon)+t_{\chi}^{2}(\varepsilon)\right)\right]}{2\sigma_{c}^{L}r_{c}^{2}t_{\chi}(\varepsilon)+2\sigma_{int,\chi}(\varepsilon)\left(2r_{c}t_{\chi}(\varepsilon)+t_{\chi}^{2}(\varepsilon)\right)t_{\chi}(\varepsilon)+\sigma_{int,\chi}(\varepsilon)L\left(r_{c}+t_{\chi}(\varepsilon)\right)^{2}}, \tag{64a}$$

$$\tilde{\sigma}_{\chi}^{T}(\varepsilon)=\frac{\sigma_{int,\chi}(\varepsilon)}{L+2t_{\chi}(\varepsilon)}\left[L\frac{2r_{c}^{2}\sigma_{c}^{T}+\left(\sigma_{c}^{T}+\sigma_{int,\chi}(\varepsilon)\right)\left(t_{\chi}^{2}(\varepsilon)+2r_{c}t_{\chi}(\varepsilon)\right)}{2r_{c}^{2}\sigma_{int,\chi}(\varepsilon)+\left(\sigma_{c}^{T}+\sigma_{int,\chi}(\varepsilon)\right)\left(t_{\chi}^{2}(\varepsilon)+2r_{c}t_{\chi}(\varepsilon)\right)}+2t_{\chi}(\varepsilon)\right] \tag{64b}$$

with σ_c^L and σ_c^T being the longitudinal and transverse electrical conductivities of the CNTs. Given that the dimensions of the equivalent composite cylinders are larger than the original CNTs, the volume fraction of the inclusions must be updated. The volume fraction f_{eff} of the effective solid fillers, i.e. fillers and interphases, reads:

$$f_{eff,\chi}(\varepsilon)=\frac{\left(r_{c}+t_{\chi}(\varepsilon)\right)^{2}\left(L+2t_{\chi}(\varepsilon)\right)}{r_{c}^{2}L}f(\varepsilon) \tag{65}$$

with L and r_c being the length and the radius of the CNTs.

This formulation can be readily implemented in the theoretical formulation presented in Section 3 by considering the electrical conductivities given by Eq. (64). To do so, note that simply one should consider the electron hopping and the conductive networking ($s \to \infty$) mechanisms as the non-percolating and the percolating phases of the model.

Finally, it is important to remark that the previous formulation assumes CNTs as straight fibers. Such an hypothesis may be unrealistic in many cases, since CNTs usually take curved geometries during the mixing procedure due to their low bending stiffness and high aspect ratio. An example of this is given in Fig. 18, which shows a scanning electron microscope (SEM) picture of multi-walled CNTs (MWCNTs) in water suspension. In this light, several geometrical approaches to model the waviness effects of CNTs can be found in the literature, including planar sinusoidal curves, helixes, and polylines with straight segments [71]. Nonetheless, these curved geometries can be straightforwardly introduced into the presented micromechanics formulation following the equivalent straight fiber approach by Takeda and co-authors [64]. The basic idea is that wavy CNTs of length L^{wavy} can be converted to equivalent straight fibers of length L^{str} with the capability of: (i) conducting the same electric flux; and (ii) transporting the same amount of electric charges. The first condition implies that, when subjected to a potential difference ΔV, the electrical flux J remains the same for both wavy and equivalent straight fillers. This relation can be approximated as [54]:

$$J=\sigma_{c}\frac{\Delta V}{L^{wavy}}=\sigma_{c}^{str}\frac{\Delta V}{L^{str}}, \tag{66}$$

which leads to the effective electrical conductivity of the equivalent straight fibers as $\sigma_c^{str} = \kappa\sigma_c$, with $\kappa = L^{str}/L^{wavy}$ being their lengths ratio. On the other hand, the second condition imposes the same electrical charge through the wavy and the equivalent straight fillers and, therefore, the same electrical resistance, i.e. $R_{cnt}^{str} = R_{cnt}^{wavy}$. On this basis, considering CNTs as ideal cylindrical conductors, it is trivially extracted that wavy and equivalent straight CNTs must have the same cross-section. Therefore, the volume fraction of the equivalent straight fibers can be computed as $f^{str} = \kappa f$. It follows that waviness ratio κ suffices to determine the electrical conductivity tensor of the equivalent straight fillers. Note that the length of the equivalent straight fibers L^{str}, and thus κ, depends upon the considered wavy geometry. Interested readers can find the explicit micromechanics formulation of the electrical conductivity of CNT-based composites considering helical wavy geometries in Ref. [19].

Appendix B. Supplementary data

Supplementary Material 1 of this article can be found online at https://doi.org/10.1016/j.carbon.2021.08.083

References

[1] G.M. Koo, T.N. Tallman, Frequency-dependent alternating current piezoresistive switching behavior in self-sensing carbon nanofiber composites, Carbon 173 (2021) 384–394.

[2] X. Sun, J. Sun, T. Li, S. Zheng, C. Wang, W. Tan, J. Zhang, C. Liu, T. Ma, Z. Qi, C. Liu, N. Xue, Flexible tactile electronic skin sensor with 3D force detection based on porous CNTs/PDMS nanocomposites, Nano-Micro Lett. 11 (2019) 1–14.

[3] H. Ghaednia, C.E. Owens, R. Roberts, T.N. Tallman, A.J. Hart, K.M. Varadarajan, Interfacial load monitoring and failure detection in total joint replacements via piezoresistive bone cement and electrical impedance tomography, Smart Mater. Struct. 29 (8) (2020), 085039.

[4] A. Liu, Z. Ni, J. Chen, Y. Huang, Highly sensitive graphene/polydimethylsiloxane composite films near the threshold concentration with biaxial stretching, Polymers 12 (2020) 71.

[5] D. Song, X. Li, X.P. Li, X. Jia, P. Min, Z.Z. Yu, Hollow-structured MXene-PDMS composites as flexible, wearable and highly bendable sensors with wide working range, J. Colloid Interface Sci. 555 (2019) 751–758.

[6] M.S. Irfan, T. Khan, T. Hussain, K. Liao, R. Umer, Carbon coated piezoresistive fiber sensors: from process monitoring to structural health monitoring of composites–A review, Compos. Appl. Sci. Manuf. 141 (2021) 106236.

[7] L. Chang, K. Friedrich, L. Ye, P. Toro, Evaluation and visualization of the percolating networks in multi-wall carbon nanotube/epoxy composites, J. Mater. Sci. 44 (2009) 4003–4012.

[8] Z.H. Tang, Y.Q. Li, P. Huang, Y.Q. Fu, N. Hu, S.Y. Fu, A new analytical model for predicting the electrical conductivity of carbon nanotube nanocomposites, Composites Communications 23 (2021) 100577.

[9] Y. Fang, L.Y. Li, S.H. Jang, Calculation of electrical conductivity of self-sensing carbon nanotube composites, Compos. B Eng. 199 (2020) 108314.

[10] E. García-Macías, R. Castro-Triguero, A. Sáez, F. Ubertini, 3D mixed micromechanics-FEM modeling of piezoresistive carbon nanotube smart concrete, Comput. Methods Appl. Mech. Eng. 340 (2018) 396–423.

[11] Y. Wang, G.J. Weng, S.A. Meguid, A.M. Hamouda, A continuum model with a percolation threshold and tunneling-assisted interfacial conductivity for carbon nanotube-based nanocomposites, J. Appl. Phys. 115 (2014) 193706.

[12] R. Hashemi, G.J. Weng, A theoretical treatment of graphene nanocomposites with percolation threshold, tunneling-assisted conductivity and microcapacitor effect in AC and DC electrical settings, Carbon 96 (2016) 474–490.

[13] C. Feng, Li Jiang, Micromechanics modeling of the electrical conductivity of carbon nanotube (CNT)–polymer nanocomposites. Composites Part A: applied Science and Manufacturing, Compos. Appl. Sci. Manuf. 47 (2013) 143–149.

[14] E. García-Macías, A. Downey, A. D'Alessandro, R. Castro-Triguero, S. Laflamme, F. Ubertini, Enhanced lumped circuit model for smart nanocomposite cement-based sensors under dynamic compressive loading conditions, Sensor Actuator Phys. 260 (2017) 45–57.

[15] B. Han, K. Zhang, X. Yu, E. Kwon, J. Ou, Electrical characteristics and pressure-sensitive response measurements of carboxyl MWNT/cement composites, Cement Concr. Compos. 1 (34) (2021) 794–800.

[16] A. D'Alessandro, F. Ubertini, A.L. Materazzi, S. Laflamme, M. Porfiri, Electromechanical modelling of a new class of nanocomposite cement-based sensors for structural health monitoring, Struct. Health Monit. (2014), 1475921714560071.

[17] A. Gbaguidi, S. Namilae, D. Kim, Stochastic percolation model for the effect of nanotube agglomeration on the conductivity and piezoresistivity of hybrid nanocomposites, Comput. Mater. Sci. 166 (2019) 9–19.
[18] S. Wang, Y. Huang, E. Chang, C. Zhao, A. Ameli, H.E. Naguib, C.B. Park, Evaluation and modeling of electrical conductivity in conductive polymer nanocomposite foams with multiwalled carbon nanotube networks, Chem. Eng. J. 411 (2021) 128382.
[19] E. García-Macías, A. D'Alessandro, R. Castro-Triguero, D. Pérez-Mira, F. Ubertini, Micromechanics modeling of the electrical conductivity of carbon nanotube cement-matrix composites, Compos. B Eng. 108 (2017) 451–469.
[20] C. Feng, L.Y. Jiang, Investigation of uniaxial stretching effects on the electrical conductivity of CNT–polymer nanocomposites, J. Phys. Appl. Phys. 47 (2014) 405103.
[21] T. Tallman, K.W. Wang, An arbitrary strains carbon nanotube composite piezoresistivity model for finite element integration, Appl. Phys. Lett. 102 (2013), 011909.
[22] N. Hu, Y. Karube, C. Yan, Z. Masuda, H. Fukunaga, Tunneling effect in a polymer/carbon nanotube nanocomposite strain sensor, Acta Mater. 56 (2008) 2929–2936.
[23] L.Y. Alamusi, N. Hu, Numerical simulations on piezoresistivity of CNT/polymer based nanocomposites, Comput. Mater. Continua (CMC) 20 (2010) 101–117.
[24] J.G. Simmons, Generalized formula for the electric tunnel effect between similar electrodes separated by a thin insulating film, J. Appl. Phys. 34 (6) (1964) 1793–1803.
[25] M. Taya, W.J. Kim, K. Ono, Piezoresistivity of a short fiber/elastomer matrix composite, Mech. Mater. 28 (1998) 53–59.
[26] C. Feng, L. Jiang, Micromechanics modeling of bi-axial stretching effects on the electrical conductivity of CNT-polymer composites, Int. J. Appl. Mech. 7 (2015) 1550005.
[27] E. García-Macías, A. D'Alessandro, R. Castro-Triguero, D. Pérez-Mira, F. Ubertini, Micromechanics modeling of the uniaxial strain-sensing property of carbon nanotube cement-matrix composites for SHM applications, Compos. Struct. 163 (2017) 195–215.
[28] Y. Fang, L.Y. Li, S.H. Jang, Piezoresistive modelling of CNTs reinforced composites under mechanical loadings, Compos. Sci. Technol. 208 (2021) 108757.
[29] Z.H. Tang, Y.Q. Li, P. Huang, H. Wang, N. Hu, S.Y. Fu, Comprehensive evaluation of the piezoresistive behavior of carbon nanotube-based composite strain sensors, Compos. Sci. Technol. 208 (2021) 108761.
[30] M.A.S. Matos, V.L. Tagarielli, P.M. Baiz-Villafranca, S.T. Pinho, Predictions of the electro-mechanical response of conductive CNT-polymer composites, J. Mech. Phys. Solid. 114 (2018) 84–96.
[31] J. Wang, W. Wang, C. Zhang, W. Yu, The electro-mechanical behavior of conductive filler reinforced polymer composite undergone large deformation: a combined numerical-analytical study, Compos. B Eng. 133 (2018) 185–192.
[32] H. Yang, L. Yuan, X. Yao, D. Fang, Piezoresistive response of graphene rubber composites considering the tunneling effect, J. Mech. Phys. Solid. 139 (2020) 103943.
[33] T. Komori, K. Makishima, Numbers of Fiber-To-Fiber Contacts in General Fiber Assemblies Textile Research Journal, vol. 47, SAGE Publications, 1977, pp. 13–17.
[34] F. Peter, H. Weyl, Die vollständigkeit der primitiven darstellungen einer geschlossenen kontinuierlichen gruppe, Math. Ann. 97 (1927) 737–755.
[35] I.M. Gel'fand, R.A. Minlos, G. Cummins, Representations of the Rotation and Lorentz Groups and Their Applications, Macmillan, 1963.
[36] H. Bunge, Texture Analysis in Materials Science, Butterworths, London, 1982.
[37] U.F. Kocks, C.N. Tomé, H.-R. Wenk, Texture and Anisotropy. Preferred Orientations in Polycrystals and Their Effect on Materials Properties, Cambridge University Press, 2005.
[38] M.L. Dunn, H. Ledbetter, Thermal expansion of textured polycrystalline aggregates, J. Appl. Phys. 78 (1995) 1583–1588.
[39] J.Y. Li, M.L. Dunn, H. Ledbetter, Thermoelectroelastic moduli of textured piezoelectric polycrystals: exact solutions and bounds for film textures, J. Appl. Phys. 86 (1999) 4626–4634.
[40] J.Y. Li, The effective electroelastic moduli of textured piezoelectric polycrystalline aggregates, J. Mech. Phys. Solid. 48 (2000) 529–552.
[41] J.L. Buroni, F.C. Buroni, A.P. Cisilino, R. Melnik, L. Rodríguez-Tembleque, A. Sáez, Analytical expressions to estimate the effective piezoelectric tensor of a textured polycrystal for any crystal symmetry, Mech. Mater. 151 (2020) 103604.
[42] M. Ferrari, G.C. Johnson, The equilibrium properties of a 6 mm polycrystal exhibiting transverse isotropy, J. Appl. Phys. 63 (1988) 4460–4468.
[43] M.L. Dunn, H. Ledbetter, P.R. Heyliger, C. Sun-Choi, Elastic constants of textured short-fiber composites, J. Mech. Phys. Solid. 44 (1996) 1509–1541.
[44] M.L. Dunn, H. Ledbetter, Elastic-plastic behavior of textured short-fiber composites, Acta Mater. 45 (1997) 3327–3340.
[45] M.L. Dunn, H. Ledbetter, Micromechanically-based acoustic characterization of the fiber orientation distribution function of morphologically textured short-fiber composites: prediction of thermomechanical and physical properties, Materials Science and Engineering: A. 285 (2000) 56–61.
[46] J.A. Krishnaswamy, F.C. Buroni, F. Garcia-Sanchez, R. Melnik, L. Rodriguez-Tembleque, A. Sáez, Improving the performance of lead-free piezoelectric composites by using polycrystalline inclusions and tuning the dielectric matrix environment, Smart Mater. Struct. 28 (2019), 075032.
[47] J.A. Krishnaswamy, F.C. Buroni, F. Garcia-Sanchez, R. Melnik, L. Rodriguez-Tembleque, A. Sáez, Lead-free piezocomposites with CNT-modified matrices: accounting for agglomerations and molecular defects, Compos. Struct. 224 (2019) 111033.
[48] J.A. Krishnaswamy, F.C. Buroni, E. García-Macías, R. Melnik, L. Rodriguez-Tembleque, A. Sáez, Design of nano-modified PVDF matrices for lead-free piezocomposites: graphene vs carbon nanotube nano-additions, Mech. Mater. 142 (2020) 103275.
[49] J.A. Krishnaswamy, F.C. Buroni, R. Melnik, L. Rodriguez-Tembleque, A. Sáez, Size dependent electro-elastic enhancement in geometrically anisotropic lead-free piezocomposites, Int. J. Mech. Sci. 182 (2020) 105745.
[50] J.A. Krishnaswamy, F.C. Buroni, R. Melnik, L. Rodriguez-Tembleque, A. Sáez, Design of polymeric auxetic matrices for improved mechanical coupling in lead-free piezocomposites, Smart Mater. Struct. 29 (2020), 054002.
[51] J.A. Krishnaswamy, F.C. Buroni, R. Melnik, L. Rodriguez-Tembleque, A. Sáez, Multiscale design of nanoengineered matrices for lead-free piezocomposites: improved performance via controlling auxeticity and anisotropy, Compos. Struct. 255 (2021) 112909.
[52] R.-J. Roe, Description of crystallite orientation in polycrystalline materials. III. General solution to Pole figure inversion, J. Appl. Phys. 36 (1965) 2024.
[53] T. Mori, K. Tanaka, Average stress in matrix and average elastic energy of materials with misfitting inclusions, Acta Metall. 21 (1973) 571–574.
[54] F. Deng, Q.S. Zheng, An analytical model of effective electrical conductivity of carbon nanotube composites, Appl. Phys. Lett. 92 (2008), 071902.
[55] T. Mura, Micromechanics of Defects in Solids, Second, revised edition, Martinus Nijhoff Publishers, Dordrecht, 1987.
[56] Mathematica, Version 12.1, Wolfram Research, Inc., Champaign IL, 2020.
[57] E. García-Macías, L. Rodríguez-Tembleque, A. Sáez, F. Ubertini, Crack detection and localization in RC beams through smart MWCNT/epoxy strip-like strain sensors, Smart Mater. Struct. 27 (2018) 115022.
[58] E. García-Macías, F. Ubertini, Earthquake-induced damage detection and localization in masonry structures using smart bricks and Kriging strain reconstruction: a numerical study, Earthq. Eng. Struct. Dynam. 48 (2019) 548–569.
[59] V. Kumar, A. Rawal, Tuning the electrical percolation threshold of polymer nanocomposites with rod-like nanofillers, Polymer 97 (2016) 295–299.
[60] MATLAB, 9.4.0.949201 (R2018a). Natick, Massachusetts, The MathWorks Inc, 2018.
[61] G. Van Rossum, F.L. Drake, Python 3 Reference Manual, Scotts Valley, CreateSpace, CA, 2009.
[62] E.T. Thostenson, Z. Ren, T.W. Chou, Advances in the science and technology of carbon nanotubes and their composites: a review, Compos. Sci. Technol. 61 (2001) 1899–1912.
[63] M.Y. Hwang, D.H. Han, L.H. Kang, Piezoresistive multi-walled carbon nanotube/epoxy strain sensor with pattern design, Materials 12 (2019) 3962.
[64] T. Takeda, Y. Shindo, Y. Kuronuma, F. Narita, Modeling and characterization of the electrical conductivity of carbon nanotube-based polymer composites, Polymer 52 (2011) 3852–3856.
[65] G.D. Seidel, D.C. Lagoudas, A micromechanics model for the electrical conductivity of nanotube-polymer nanocomposites, J. Compos. Mater. 43 (2009) 917–941.
[66] E. García-Macías, F. Ubertini, Book Chapter: 5 - Mathematical Modeling and Simulation. Smart Nanoconcretes and Cement-Based Materials. Micro and Nano Technologies, 2020, pp. 101–156.
[67] N. Mishra, K. Das, A mori–Tanaka based micromechanical model for predicting the effective electroelastic properties of orthotropic piezoelectric composites with spherical inclusions, SN Applied Sciences 2 (7) (2020) 1–14.
[68] T. Kil, D.W. Jin, B. Yang, H.K. Lee, A comprehensive micromechanical and experimental study of the electrical conductivity of polymeric composites incorporating carbon nanotube and carbon fiber, Compos. Struct. 268 (2021) 114002.
[69] N. Tassi, A. Bakkali, N. Fakri, L. Azrar, A. Aljinaidi, Well conditioned mathematical modeling for homogenization of thermo-electro-mechanical behaviors of piezoelectric composites, Appl. Math. Model. 99 (2021) 276–293.
[70] A. Sanli, C. Müller, O. Kanoun, C. Elibol, M.F.X. Wagner, Piezoresistive characterization of multi-walled carbon nanotube-epoxy based flexible strain sensitive films by impedance spectroscopy, Compos. Sci. Technol. 122 (2016) 18–26.
[71] E. García-Macías, R. Castro-Triguero, Coupled effect of CNT waviness and agglomeration: a case study of vibrational analysis of CNT/polymer skew plates, Compos. Struct. 193 (2018) 87–102.